LABORATÓRIO NACIONAL
DE ENGENHARIA CIVIL

CODE IMPLEMENTATION OF PARTICLE BASED DISCRETE ELEMENT METHOD FOR CONCRETE VISCOELASTIC MODELLING

Estudo realizado no âmbito do projeto DamConcrete
do P2I do LNEC

Lisboa • outubro de 2015

I&D BARRAGENS DE BETÃO

RELATÓRIO 333/**2015 – DBB/NO**

Título

CODE IMPLEMENTATION OF PARTICLE BASED DISCRETE ELEMENT METHOD FOR CONCRETE VISCOELASTIC MODELLING

Autoria

DEPARTAMENTO DE BARRAGENS DE BETÃO

Carlos Serra
Bolseiro de Doutoramento, Núcleo de Observação

Nuno Monteiro Azevedo
Investigador Auxiliar, Núcleo de Modelação e Mecânica das Rochas

António Lopes Batista
Investigador Principal, Diretor do Departamento

AV DO BRASIL 101 • 1700-066 LISBOA

e-mail: lnec@lnec.pt

www.lnec.pt

Relatório 333/2015

Proc. 0403/112/20181, 0401/112/2018101, 0402/112/2018102

CODE IMPLEMENTATION OF PARTICLE BASED DISCRETE ELEMENT METHOD FOR CONCRETE VISCOELASTIC MODELLING

Abstract

This report describes the application of discrete element method to rigid particle models and proposes the use of the discrete element method for the modelling of the behaviour of concrete, namely the time-independent and time-dependent or instantaneous and delayed behaviour. The main goals of this work are: i) the implementation of a discrete element method code using rigid particles; and ii) the implementation of constitutive contact models for the delayed behaviour of concrete.

Elastic, viscoelastic and aging models were implemented and several examples were used to validate the method. A fast numerical simulation scheme for the creep behaviour was applied to decrease the computational effort over large loading times for the analysis of concrete behaviour.

Keywords: Discrete element method / Rigid particle model / Dynamic relaxation / Viscoelastic behaviour / Solidification theory

IMPLEMENTAÇÃO NUMÉRICA DO MÉTODO DOS ELEMENTOS DISCRETOS APLICADO A MODELOS DE PARTÍCULAS PARA A MODELAÇÃO DO COMPORTAMENTO VISCOELÁSTICO DO BETÃO

Resumo

Neste trabalho descreve-se a utilização do método dos elementos discretos para a modelação do comportamento do betão, nomeadamente para o comportamento instantâneo e diferido. Os principais objetivos são: i) a implementação do método dos elementos discretos aplicado a modelos de partículas rígidas através de um programa de computador; e ii) a implementação de modelos constitutivos no contacto para a modelação do comportamento diferido do betão.

Foram implementados modelos de contacto elásticos, viscoelásticos e viscoelásticos com endurecimento, tendo sido utilizados vários exemplos para a validação do método. Foi desenvolvida, também, uma metodologia numérica para uma análise dos efeitos de fluência do betão de forma a diminuir o esforço computacional para análises com longos períodos de carregamento.

Palavras-chave: Método dos elementos discretos / Modelo de partículas / Relaxação dinâmica / Comportamento viscoelástico / Teoria da solidificação

Contents

List of Figures

List of Tables

1| Introduction

1.1 Scope and objectives

The presented report describes part of the work developed for the Ph. D. thesis of the grant holder Carlos Serra, entitled "Experimental characterization and numerical modelling of dam concrete rheological properties" which started in 2013 [Serra et al., 2013]. It is proposed the use of the discrete element method for the modelling of the behaviour of concrete, namely the time-independent and time-dependent or instantaneous and delayed behaviour. Bearing the objectives of the thesis., the main goals of this work are:

1. the implementation of a discrete element method code using rigid particles;
2. the implementation of constitutive contact models for the delayed behaviour of concrete.

The main purpose of the developed particle based discrete element method is to test different constitutive models for the further study of complex concrete systems. Regarding those tests, three types of constitutive models were implemented: 1) the elastic time-independent behaviour based on the Hooke's model; 2) a viscoelastic time-dependent behaviour based on the Burger model; and 3) an aging time-dependent model based on the solidification theory.

The implemented particle based discrete element method relies on a explicit time-stepping scheme and therefore the time-step is bounded by a small value, which can be very time-consuming for the study of long-term behaviour of concrete. To overcome this constraint, a numerical scheme for fast simulation of time-dependent behaviour was also introduced into the particle model.

The present report is organized into five chapters, namely this "Introduction", a "Literature review", with the discussion of the different types of discrete models considered in this report, a chapter describing the implemented "Particle based discrete element method", the "Verification of the code implementation" with several examples and the "Conclusions".

1.2 Framework

The initial framework of this study was the development of a numerical implementation for the analysis of a structural system in the context of the doctoral course of the *Faculdade de Ciências e Tecnologia* of the *Universidade Nova de Lisboa* entitled *Elementos finitos em engenharia de estruturas*, under Prof. Corneliu Cismasiu's supervision.

2| Literature review

2.1 General aspects

The quasi-brittle behaviour of some heterogeneous materials is considered to be poorly simulated by continuous approaches that disregard the material microstruture and the randomness of material heterogeneity [Azevedo, 2003]. The damage and fracture processes of this type of materials are complex and sensitive to the area where the energy is dissipating and, therefore, numerical models should consider this effect [Bažant, 2002].

Discrete models are able to introduce some type of microstructure and randomness into the model and the cracking zone is explicitly taken into consideration. By considering the material as a randomly produced assembly of discrete rigid particles in contact with each other and, for those contacts, consider a simple interaction model, it is possible to take into account the former effects.

Rigid particle models, initially developed for modelling granular materials, are being used to reproduce the overall behaviour of quasi-brittle materials, such as rock and concrete, and have been shown to reproduce several macroscopic phenomena, such as elasticity, viscoelasticity, post-peak behaviour, crack propagation and strength increase with confinement.

2.2 Discrete models

The use of distinct or discrete element method (DEM) was first applied to the study of geotechnical materials of granular nature. The work of Cundall in 1971 show the basis for the DEM simulation by considering the movement and interaction of rock blocks [Cundall, 1971]. In 1979, Cundall and Strack proposed a 2D circular particle model, validated with the experimental study of Josselin de Jong and Verruijt for a physical assembly of disks [Cundall and Strack, 1979]. Other models were developed in this period considering similar hypotheses [Rodríguez-Ortiz, 1974; Kawai, 1978].

Later on, cracking was taken into account for geomaterials, such as rock, with very simple contact models between rigid elements [Zubelewicz and Mróz, 1983; Plesha, 1983]. Plesha [1983] focused on the importance of the rock microstruture and proposed a model explicitly considering the microstruture into the interaction of discrete rigid polygons or polyhedra. At a larger scale problem, Vieria de Lemos [1987] applied the method to the dynamic analysis of rock mass of dam foundations using polyhedra.

Bažant et al. [1990] proposed a model where pin-jointed frames are connect to the centres of the aggregates and therefore the dimension of the frames are linked to the mesostructure of the material. Cusatis [2001] presented a tridimensional particle model where coarse aggregates are explicitly modelled as rigid particles and the interaction between them simulates the cement paste or mortar.

The lattice models considering bending frames [Schlangen and van Mier, 1992] differ from the lattice models proposed by Bažant et al. [1990] since the former use the finite element method (FEM) and the

latter use the distinct or discrete element method (DEM) for obtaining the response. The former models solve the equilibrium equations, by assembling the stiffness matrix of the system, at each time step. The latter method is based on a numerical time integration scheme for solving the equations of motion and for the definition of contact interaction between elements.

Within discrete models, there are the lattice models where the material is discretized as a random mesh of interconnected frames, with or without bending stiffness. The dimension of the frames is related to the heterogeneity of the material. The global behaviour, including damage and failure, is obtained by removing the frames that reach a maximum strength stress as load increases [Schlangen and van Mier, 1992]. Some work has been done improving this types of models [Lilliu and van Mier, 2003].

Rigid-body-spring networks have been also used to model the overall behaviour of structures [Kawai, 1978] and the behaviour of concrete [Bolander and Saito, 1998]. These models require the definition of the interaction springs between rigid bodies at their interface.

The present work refers to the use of discrete element method (DEM) with a rigid circular particle model. The main developments of this type of models are due to Cundall, which is still actively working in modelling the behaviour of rock mass [Mas Ivars et al., 2011]. In fact, DEM has been used to simulate granular and cohesive material, with the aid of several types of constitutive models. Meguro and Hakuno [1989] proposed an extended version of DEM, the modified discrete element method, MDEM, with the intent of simulating the behaviour of concrete under extreme dynamic events. The difference at that time was the interaction model used between the rigid particles, which where nonlinear normal and shear springs, called the "pore-strings".

Several other particle models where developed throughout the years, based on the main original Cundall's DEM [Cundall, 1971; Cundall and Strack, 1979] as the main solving method, but using different interaction models for different types of problems. Hassani [1998] compared the results of an assembly of circular particles with a visco-elastic model (Voigt-Kelvin model) and particular failure criteria with the results of a one-shear test. In the original rigid particle, the constitutive models used at contact involved only interaction at one point of contact and only forces where developed at each contact. However, materials such as rock present some kind of cemented granular nature which can be considered by introducing a bending stiffness at the contact. Failure occurs when maximum tensile and shear stresses at the contact, due to both force and moment developed at the contact, are exceeded [Potyondy and Cundall, 2004]. This enhancement is known to improve the main physical behaviour of rock, such as elasticity, micro-cracking and peak strength, for several test configurations: Brazilian test, uniaxial and triaxial compression test. Tavarez and Plesha [2007] used classical DEM formulation for modelling projectile penetration in concrete, with very high loading rates. Azevedo [2003] proposed a rigid particle model based on DEM for the analysis of plain and reinforced concrete, where both aggregates and reinforcement are explicitly considered. In his work, several contact models were used in order to proper simulate the dam concrete behaviour. Some work have been also done in order to evaluate the influence of the coarse aggregates on the development of stress-strain behaviour [Azevedo et al., 2008]. The post-peak tensile and shear behaviour at contact can be considered using brittle, linear or bi-linear constitutive models [Azevedo, 2003].

3| Particle based discrete element method

3.1 General aspects

The discrete element method (DEM) can be described as a numerical method for solving structural systems of individual elements, blocks (polygons) or particles (circular or spherical) interacting with each other at contact points or interfaces. Each element, usually considered to be rigid, is ruled by a motion law and each contact by an interaction law. The motion law defines the differential equation that governs the kinematic of the elements. This differential equation is given by the Newton's second law of motion. The interaction law, known as the force-displacement law, determines the interaction forces between particles at the contact point, according with their relative displacement. The unbalanced force of each element at a given time is used for setting new velocities and positions using the law of motion, and, therefore, new interaction forces.

The advantages of this type of method is the possibility to have large displacements and rotations, the complete detachment of two elements when their contact reaches its strength capacity and consider new contacts during the simulation [Azevedo, 2003]. Figure 3.1 illustrates a complete DEM cycle with the update of the forces and displacements of each element, in between the force-displacement law and the law of motion. The force-displacement law defines the contact interaction model and gives the response of incremental forces for the correspondent incremental displacements. The law of motion introduces the differential equation that governs the movement of each particle, based on the Newton's law of motion and through numerical integration of the accelerations.

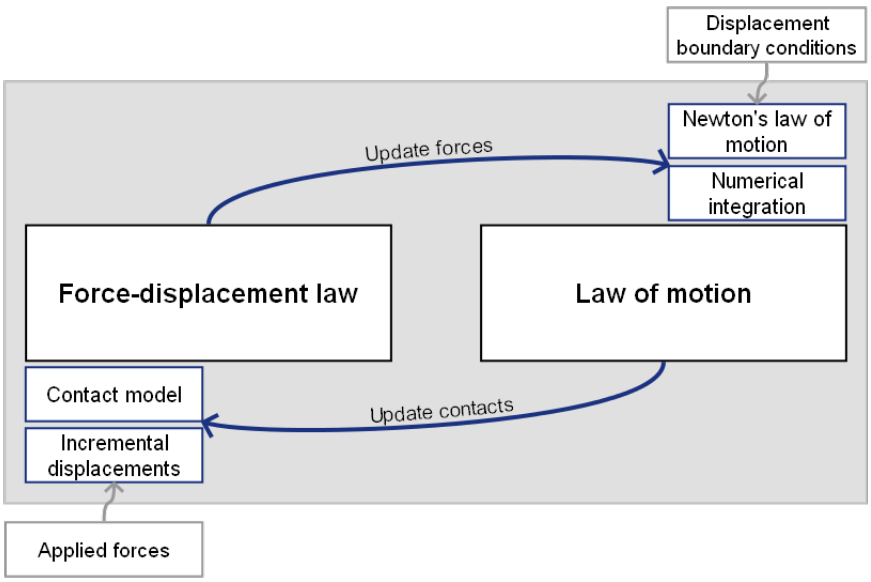

Figure 3.1 – General DEM cycle

Considering external applied forces or imposed deformations and predefined boundary conditions it is possible to calculate the response of the system using a method for solving the differential equation in

each cycle. The numerical methods commonly used for this type of problems rely on explicit integration schemes, where the solution at a given time is predicted from the response at the former time-step. In DEM, the explicit integration scheme is used for the integration of accelerations into velocities.

3.2 Two-dimensional rigid particles

This work concerns the particular case of DEM applied to two-dimensional rigid particles. The elements interacting with each other are therefore circular rigid particles defined by a position in space and a given radius (Figure 3.2). With this type of element, the contact detection and the general cycle calculations are easier to implement and require less computational time.

For this report the basis of DEM applied to two-dimensional rigid particles is presented and the following topics are discussed:

1. Force-displacement law and law of motion;
2. Explicit time-integration algorithms, namely the central difference method;
3. Stability of the solution in explicit schemes and the mechanical time step determination;
4. Types of damping;
5. Convergence criteria;
6. Micro-macro relationships and comparison with elasticity theory;
7. Contact constitutive models.

3.3 Force-displacement law

The force-displacement law or law of forces defines the behaviour of each contact between particles. When a contact between two particles is identified (Point C in Figure 3.2), the subsequent incremental relative displacements generates a contact force increment, which is applied to the centre of the particles. The contact overlap is the superposition of each particle on one another and the general convention considers compression forces related to positive contact overlap and tension forces for negative contact overlap.

The distance between particle A and particle B, d, is given by Euclidean distance between the two centres of gravity, $\mathbf{x}^{[A]}$ and $\mathbf{x}^{[B]}$, and the contact overlap, U_n, is obtained by the difference of the sum of both radius and the distance between particles.

$$d = \sqrt{\sum_{i=1}^{2} \left(x_i^{[B]} - x_i^{[A]} \right)^2} \tag{1}$$

$$U_n = R^{[A]} + R^{[B]} - d \tag{2}$$

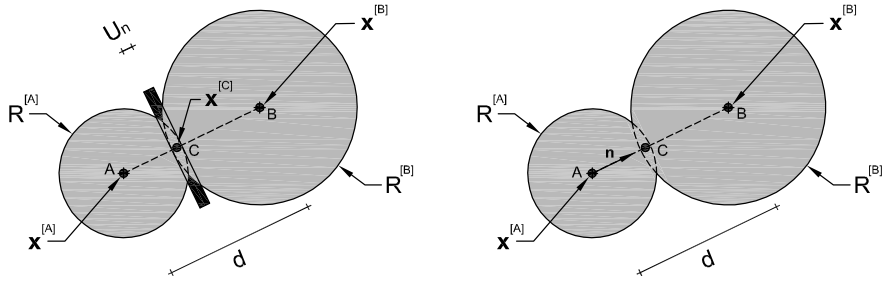

Figure 3.2 – Contact point definition

With the definition of the contact overlap and calculating the unit normal to the contact plane, $\mathbf{n}$, one can obtain the contact point location, $\mathbf{x}^{[C]}$.

$$n_i = \frac{\left(x_i^{[B]} - x_i^{[A]}\right)}{d} \tag{3}$$

$$x_i^{[C]} = x_i^{[A]} + \left(R^{[A]} - \frac{1}{2}U^n\right) n_i \tag{4}$$

The contact velocity, $\dot{\mathbf{x}}^{[C]}$ is defined by the relative velocity of both particles involved, A and B, at the contact point, $\left(\dot{\mathbf{x}}^{[C]}\right)_A$ and $\left(\dot{\mathbf{x}}^{[C]}\right)_B$. The dot above the position, $\mathbf{x}$, denotes the first derivative with respect to time and the bold refers to a vector with two components.

$$\dot{\mathbf{x}}^{[C]} = \left(\dot{\mathbf{x}}^{[C]}\right)_B - \left(\dot{\mathbf{x}}^{[C]}\right)_A \tag{5}$$

By its turn, the velocity of the particle Φ at the contact point, $\left(\dot{\mathbf{x}}^{[C]}\right)_\Phi$, (translational velocity) is given by,

$$\left(\dot{x}_i^{[C]}\right)_\Phi = \dot{x}_i^{[\Phi]} + \epsilon_{i3k}\omega_3^{[\Phi]}\left(x_k^{[C]} - x_k^{[\Phi]}\right) \tag{6}$$

$$\epsilon_{ijk} = \begin{cases} 0 & \text{if two indices coincide} \\ +1 & \text{if i.j.k permute like 1.2.3} \\ -1 & \text{otherwise} \end{cases} \tag{7}$$

where ϵ_{ijk} is the permutation symbol and $\omega_3^{[\Phi]}$ is the rotational velocity of particle Φ. In Figure 3.3 the velocities of each particle and of the contact are represented.

The displacement increment of the contact, $\Delta\mathbf{x}^{[C]}$, for a given time increment, Δt, is, by integration,

$$\Delta\mathbf{x}^{[C]} = \dot{\mathbf{x}}^{[C]}\Delta t \tag{8}$$

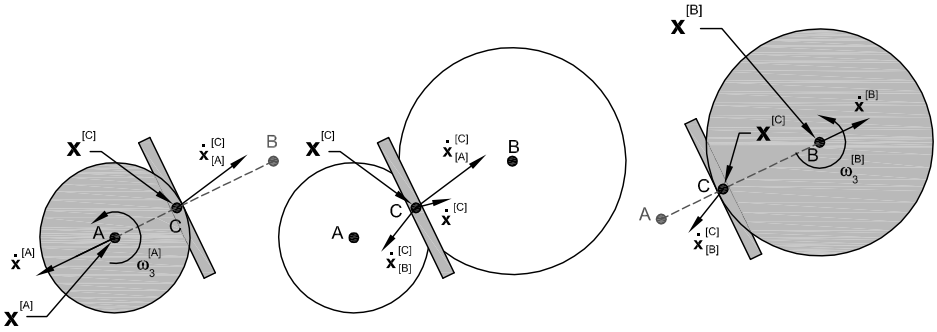

Figure 3.3 – Contact point velocity definition

and can be decomposed into the normal, $\Delta x_n^{[C]}$, and the shear, $\Delta \mathbf{x}_s^{[C]}$ components.

$$\Delta x_n^{[C]} = \sum_{i=1}^{2} \left(\Delta x_i^{[C]} \mathbf{n_i} \right) \tag{9}$$

$$\mathbf{\Delta x}_s^{[C]} = \Delta \mathbf{x}^{[C]} - \Delta x_n^{[C]} \mathbf{n} \tag{10}$$

The normal and shear contact force increments, $\Delta F_n^{[C]}$ and $\mathbf{\Delta F}_s^{[C]}$, are obtained from the linear constitutive law of the contact and the normal and shear contact stiffness, k_n and k_s (Figure 3.4).

$$\Delta F_n^{[C]} = -k_n \Delta x_n^{[C]} \tag{11}$$

$$\mathbf{\Delta F}_s^{[C]} = -k_s \mathbf{\Delta x}_s^{[C]} \tag{12}$$

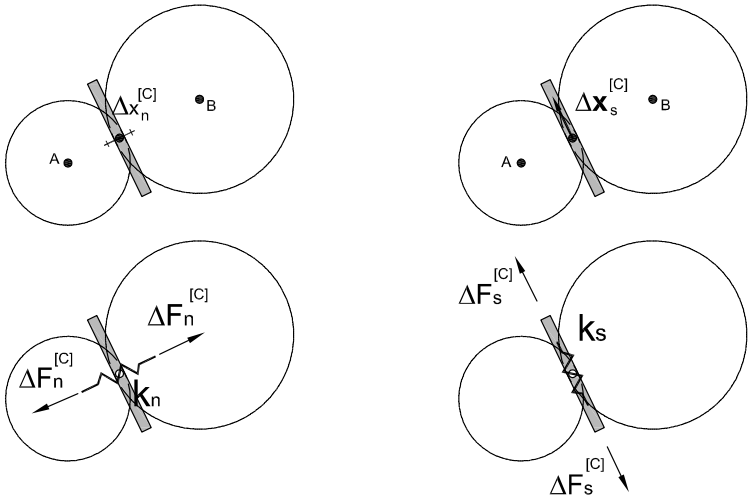

Figure 3.4 – Incremental linear contact model

Since the shear contact force is defined in global coordinates and to take into account large displacements, its necessary to correct the shear contact force to refer it to the new contact plane, between each time step, assuming infinitesimal rotations. Figure 3.5 shows the corrected shear force referred to the new contact plane.

$$\mathbf{\Delta F}_s^{[C],corrected} = \mathbf{\Delta F}_s^{[C],old} - \epsilon_{ij3}\epsilon_{3mn}\mathbf{\Delta F}_j^{[C],old}\mathbf{n}_j^{old}n_n \tag{13}$$

and, therefore, the updated predicted normal and shear forces at contact point are obtained from,

$$F_n^{[C]} = F_n^{[C],old} + \Delta F_n^{[C]} \tag{14}$$

$$\mathbf{F_s}^{[C]} = \mathbf{F_s}^{[C],corrected} + \mathbf{\Delta F_s}^{[C]} \tag{15}$$

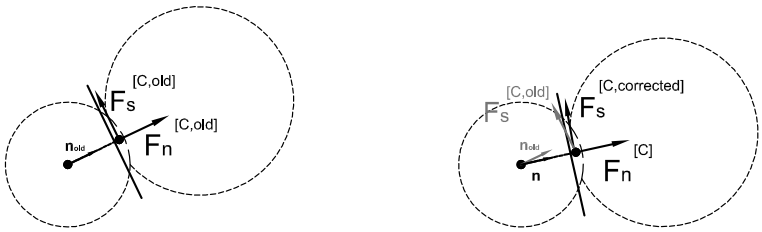

Figure 3.5 – Correction of shear contact force

The contact model is applied and then the new contact force, $\mathbf{F}^{[C]}$, is given by the vectorial sum of normal and shear components (the $\bullet$ represents the internal product between two vectors).

$$\mathbf{F}^{[C]} = F_n^{[C]} \bullet \mathbf{n} + \mathbf{F_s}^{[C]} \tag{16}$$

The contact forces, from each contact, are then transmitted and summed to both particles, obtaining the resultant internal forces and moments acting at particle centre, $\mathbf{F}_{t+1}^{[\Phi]}$ and $M_{3,t+1}^{[\Phi]}$ (Figure 3.6).

$$\mathbf{F}_{t+1}^{[A]} = \mathbf{F}_t^{[A]} - \mathbf{F}_t^{[C]} \tag{17}$$

$$\mathbf{F}_{t+1}^{[B]} = \mathbf{F}_t^{[B]} + \mathbf{F}_t^{[C]} \tag{18}$$

$$M_{3,t+1}^{[A]} = M_{3,t}^{[A]} - \epsilon_{3jk}\left(x_j^{[C]} - x_j^{[A]}\right)F_{k,t}^{[C]} \tag{19}$$

$$M_{3,t+1}^{[B]} = M_{3,t}^{[B]} + \epsilon_{3jk}\left(x_j^{[C]} - x_j^{[B]}\right) F_{k,t}^{[C]} \tag{20}$$

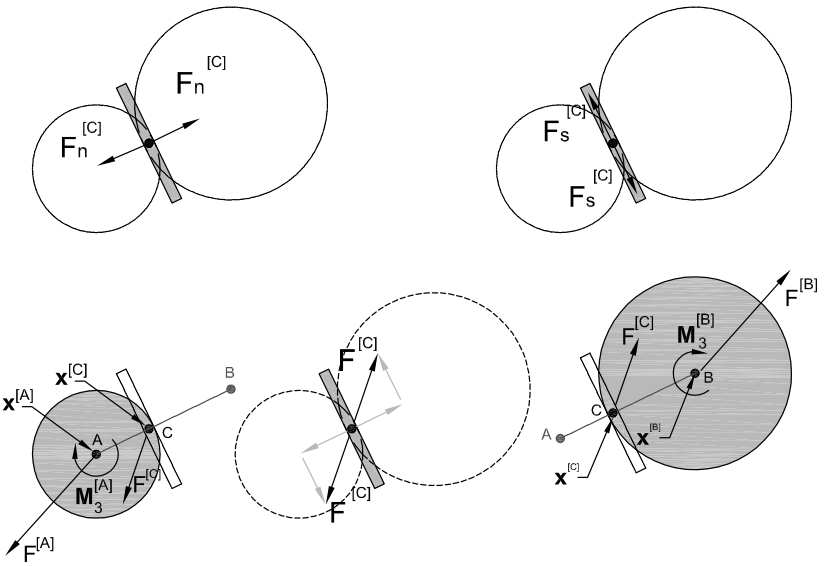

Figure 3.6 – Particles forces

3.4 Law of motion

3.4.1 Newton's second law

Newton's second law of motion defines the response of a single particle with applied forces or moments,

$$\mathbf{F}(t) = m\ddot{\mathbf{x}}(t) \tag{21}$$

$$M_3(t) = I\dot{\omega}_3(t) \tag{22}$$

where $\mathbf{F}(t)$ and $M_3(t)$ are the total applied force and moment at time t, m and I are the total mass and inertia of the particle, and $\ddot{\mathbf{x}}(t)$ and $\dot{\boldsymbol{\omega}}_{\mathbf{3}}(t)$ are the particle translational and angular accelerations. The inertia is $\beta m R^2$, where β is $2/5$ for spherical shaped particles and $1/2$ for disk shaped particles.

There are several numerical techniques for solving differential equations based on time discretization into time steps, Δt, and approximating derivatives within that discretization. Explicit methods calculate a solution at $t + \Delta t$ based only on the previous solution in t and the derivative using a time increment. The updated velocities are obtained from the accelerations using centred difference scheme for calculating derivatives.

3.4.2 Centred difference time-integration scheme

Differential equations can be numerically solved using finite difference approximations for each derivative. A derivative of the function $f(t)$ in time, t, $\dot{f}(t) = \frac{\mathrm{d}f(t)}{\mathrm{d}t}$, can be defined as limit of the slope of f within a predefined interval, Δt, when Δt tends to zero.

$$\dot{f}(t) = \frac{\mathrm{d}f(t)}{\mathrm{d}t} = \lim_{\Delta_t \to 0} \frac{f(t+\Delta t) - f(t)}{\Delta t} \tag{23}$$

One can see that, as Δt gets smaller, more accurate is the value of the derivative.

The development of a given variable, $x(t)$, in a Taylor series at time, t_0, follows,

$$x(t) = x(t_0)(t-t_0)^0 + \frac{\dot{x}(t_0)(t-t_0)^1}{1!} + \frac{\ddot{x}(t_0)(t-t_0)^2}{2!} + \frac{\dddot{x}(t_0)(t-t_0)^3}{3!} + \cdots \tag{24}$$

Taking $t = t_0 + \Delta t$ and considering $O(\Delta t^n)$ the truncated Δt^n terms of the Taylor series one can write the following expression,

$$x(t) = x(t_0)(\Delta t)^0 + \frac{\dot{x}(t_0)(\Delta t)^1}{1!} + \frac{\ddot{x}(t_0)(\Delta t)^2}{2!} + \frac{\dddot{x}(t_0)(\Delta t)^3}{3!} + \cdots \tag{25}$$

From which follow the derivative, $\dot{x}(t_0)$,

$$\dot{x}(t_0) = \frac{x(t_0+\Delta t) - x(t_0)}{\Delta t} + O(\Delta t^2) \tag{26}$$

and, therefore, the smaller the Δt, smaller the error, $O(\Delta t)$, obtained from discarding the remaining terms.

The centred difference scheme for the first derivative of $x(t)$ uses two points, $x(t-\Delta t)$ and $x(t+\Delta t)$,

$$x(t-\Delta t) = x(t_0) - \dot{x}(t_0)(\Delta t) + \frac{\ddot{x}(t_0)(\Delta t)^2}{2} - \frac{\dddot{x}(t_0)(\Delta t)^3}{6} + O(\Delta t^4) \tag{27}$$

$$x(t+\Delta t) = x(t_0) + \dot{x}(t_0)(\Delta t) + \frac{\ddot{x}(t_0)(\Delta t)^2}{2} + \frac{\dddot{x}(t_0)(\Delta t)^3}{6} + O(\Delta t^4) \tag{28}$$

The derivative, using these two points, is,

$$\begin{aligned} \dot{x}(t_0) =& \frac{x(t_0+\Delta t) - x(t_0-\Delta t)}{2\Delta t} + \frac{1}{3}\dddot{x}(t_0)\Delta t^2 + O(\Delta t^4) \\ =& \frac{x(t_0+\Delta t) - x(t_0-\Delta t)}{2\Delta t} + O(\Delta t^2) \end{aligned} \tag{29}$$

From which can be concluded that centred difference scheme gives an accuracy of $O(\Delta t^2)$ (by disregarding the Δt^2 and further terms).

For this work it will be considered that the accelerations at time t, $\ddot{\mathbf{x}}(t)$, are related to former and future velocities evaluated at mid-interval, $\dot{\mathbf{x}}(t - \Delta t/2)$ and $\dot{\mathbf{x}}(t + \Delta t/2)$, as stated by the centred difference time-integration scheme,

$$\ddot{\mathbf{x}}(t) = \frac{\dot{\mathbf{x}}^{t+\Delta t/2} - \dot{\mathbf{x}}^{t-\Delta t/2}}{2 \times \Delta t/2} \tag{30}$$

Considering Newton's second law of motion (Equation 21 and Equation 22), the velocities $\dot{x}(t + \Delta t/2)$ are obtained from,

$$\dot{\mathbf{x}}^{t+\Delta t/2} = \dot{\mathbf{x}}^{t-\Delta t/2} + \left(\frac{\mathbf{F}(t)}{m}\right)\Delta t \tag{31}$$

$$\omega_3^{t+\Delta t/2} = \omega_3^{t-\Delta t/2} + \left(\frac{\mathbf{M}_3(t)}{I}\right)\Delta t \tag{32}$$

The future position, $\mathrm{x}(t + \Delta t)$, and future rotation, $\theta(t + \Delta t)$, are given by,

$$\mathbf{x}^{t+\Delta t} = \mathbf{x}^t + \dot{\mathbf{x}}^{t+\Delta t/2}\Delta t \tag{33}$$

$$\theta^{t+\Delta t} = \theta^t + \omega_3^{t+\Delta t/2}\Delta t \tag{34}$$

Figure 3.7 is a graphical representation of the adopted central finite difference scheme. Velocities are determined at mid-interval ($t \pm \Delta t/2$) and positions are determined at primary intervals ($t \pm \Delta t$). The numerical scheme starts considering an initial value for the particle velocity at the time $t - \Delta t$, $\dot{\mathbf{x}}^{t+\Delta t/2}$ and a given external force, $F(t)$, applied to one or several particles. The unbalanced force, due to the external force, is converted into an acceleration, and using Equations 31 and 32 the new velocities can be calculated. The new positions are given by Equations 33 and 34 based on the velocities at mid-interval and the former position. The overlap is recalculated, new contact forces are derived from the contact model and new particle forces are obtained. If there are unbalanced forces, the accelerations are not null and the numerical procedure continues until convergence.

3.4.3 Global viscous damping

For a single degree of freedom damped system, with mass, m, stiffness, k, and c as the damping coefficient, the dynamic equation of motion is,

$$m\ddot{x}(t) + c\dot{x}(t) + kx(t) = 0 \tag{35}$$

Critical damping occurs when,

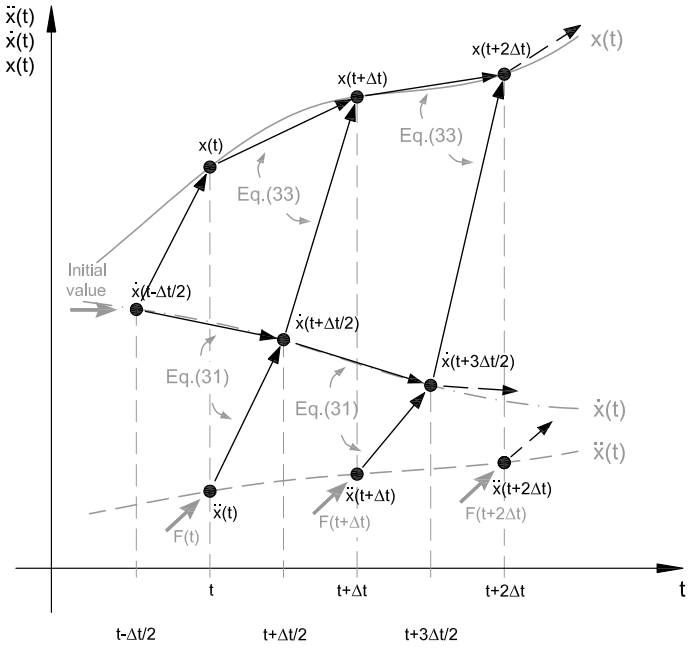

Figure 3.7 – Graphical representation of the central difference scheme

$$c = c_c = 2\omega m \tag{36}$$

where ω is the natural angular frequency [Clough and Penzien, 1993]. A damping ratio can be defined as the ratio between damping, c, and critical damping, c_c,

$$\xi = \frac{c}{c_c} \tag{37}$$

Usually dynamic systems are undercritically-damped ($c < c_c$) and, therefore, the damping ratio, ξ, is lower than 1. One can choose the value of c equal to c_c and ξ equal to unity, in order to ensure that the vibration mode is critically damped and, therefore, obtain a response that does not include oscillatory behaviour and converges faster to the steady-state position, where the unbalanced forces are null.

In N degree of freedom systems, there are N natural angular frequencies and it is difficult to choose the value of damping coefficient that ensures maximum damping efficiency. For complex systems it is usual to estimate the damping coefficient value for the lowest circular frequency, considering an undamped system,

$$c = 2\omega_0 m\xi \tag{38}$$

The equilibrium is obtained from a sum of the inertial forces and damping forces,

$$\mathbf{F}(t) = m\ddot{\mathbf{x}}(t) + c\dot{\mathbf{x}}(t) \tag{39}$$

$$M_3(t) = I\dot{\omega}_3(t) + c\omega_3(t) \tag{40}$$

For damped systems the law of motion has a viscous term in the right hand sides of Equation 31 and Equation 32 and the linear and angular velocities, $\dot{\mathbf{x}}(t)$ and $\omega_3(t)$, can be obtained from,

$$\dot{\mathbf{x}}^{t+\Delta t/2} = \left(D_1 \dot{\mathbf{x}}^{t-\Delta t/2} + \left(\frac{\mathbf{F}(t)}{m} \right) \Delta t \right) D_2 \tag{41}$$

$$\omega_3^{t+\Delta t/2} = \left(D_1 \omega_3^{t-\Delta t/2} + \left(\frac{\mathbf{M}_3(t)}{I} \right) \Delta t \right) D_2 \tag{42}$$

where $D_1 = 1 - (c/m)\Delta t/2$ and $D_2 = \frac{1}{1+(c/m)\Delta t/2}$.

3.4.4 Local non-viscous damping

Another type of damping, proposed by Cundall [1987], is the local non-viscous damping in which the damping force is proportional to the absolute value of the unbalanced force.

This results in the following expressions for the law of motion,

$$\mathbf{F}(t) + \mathbf{F}^d(t) = m\ddot{\mathbf{x}}(t) \tag{43}$$

$$M_3(t) + M_3^d(t) = I\dot{\omega}_3(t) \tag{44}$$

where $\mathbf{F}^d(t)$ and $M_3^d(t)$ are, respectively, the translational and the rotational damping forces, which can be obtained from,

$$\mathbf{F}^d(t) = -\alpha \left|\mathbf{F}(t)\right| \frac{\dot{\mathbf{x}}(t)}{\|\dot{\mathbf{x}}(t)\|} \tag{45}$$

$$M_3^d(t) = -\alpha \left|M_3(t)\right| \frac{\omega_3(t)}{\left|\omega_3(t)\right|} \tag{46}$$

The linear and angular velocities, $\dot{\mathbf{x}}(t)$ and $\omega_3(t)$, can be obtained from,

$$\dot{\mathbf{x}}^{t+\Delta t/2} = \dot{\mathbf{x}}^{t-\Delta t/2} + \left(\frac{\mathbf{F}(t) + \mathbf{F}^d(t)}{m} \right) \Delta t \tag{47}$$

$$\omega_3^{t+\Delta t/2} = \omega_3^{t-\Delta t/2} + \left(\frac{\mathbf{M}_3(t) + \mathbf{M}_3^d(t)}{I} \right) \Delta t \tag{48}$$

3.5 Stability of the solution in explicit integration schemes

3.5.1 Mechanical critical time step determination

When considering explicit time integration schemes the solution is more accurate and stable for infinitesimal time step increments and there is a critical time step for which error do not grow along the simulation. The stability of the solution along time is obtained if the chosen time step, Δt, is under this critical value, Δt_{crit} [Belytschko and Hughes, 1983].

If mass proportional damping is applied, the critical time step should be corrected to take into account the amount of damping used,

$$\Delta t \leqslant \Delta t_{crit} = \frac{2}{\omega^{max}} \left(\sqrt{1+\xi^2} - \xi \right) \tag{49}$$

where ω^{max} is the highest circular frequency of the undamped structural system and ξ is a fraction of the critical damping in the maximum frequency.

3.5.2 Gerschgorin theorem for highest circular frequency estimate

An upper bound of the maximum frequency, ω^{max}, and therefore a lower value of the critical timestep can be obtained using Gerschgorin's theorem [Underwood, 1983], which guarantees that the highest frequency of a structural system is less than or equal to the absolute ratio between the sum of the stiffness row to the sum of the mass row,

$$\omega^{max} \leq max \left\{ \sqrt{\frac{\sum_{j=1}^{n} \left| k_{ij} \right|}{m_i}} \right\} \tag{50}$$

$$\Delta t_{crit} \approx min \left\{ 2 \sqrt{\frac{m_i}{\sum_{j=1}^{n} \left| k_{ij} \right|}} \right\} \tag{51}$$

where i, j are the degrees of freedom of a row and a column of the stiffness matrix, n is the maximum number of degrees of freedom, $\sum_{j=1}^{n} \left| k_{ij} \right|$ is the absolute sum of the i^{th} row of the stiffness matrix and m_i is the generalized mass of the particle with the degree of freedom i.

A simplified approach for calculating $\sum_{j=1}^{n} \left| k_{ij} \right|$ is to consider the sum of translational (Equation 52) or rotational (Equation 54) stiffness of each particle, taking those values as the maximum bounds,

$$k^{trans} = \sum_{j=1}^{n} \left| k_{ij} \right| < \sum_{c=1}^{N_c} 2 \left(k_{n,c} + k_{s,c} \right) \tag{52}$$

$$\Delta t_{crit} \approx min \left\{ 2 \sqrt{\frac{m_i}{k^{trans}}} \right\} \tag{53}$$

$$k^{rot} = \sum_{j=1}^{n} |k_{ij}| < \sum_{c=1}^{N_c} \left(R^{[B]^2} k_{s,c} + R^{[B]} R^{[A]} k_{s,c} \right) \tag{54}$$

$$\Delta t_{crit} \approx min \left\{ 2\sqrt{\frac{I_i}{k^{rot}}} \right\} \tag{55}$$

where $(k_{n,c} + k_{s,c})$ is the sum of normal and shear stiffness of the particle, N_c is the number of contacts of the particle and R is the radius of the particle.

3.5.3 Density scaling

The mechanical critical time step, related to the maximum frequency and required for explicit time integration schemes, is usually very small which can be time consuming and computationally demanding. A way to overcome this is to use density scaling or mass scaling.

This approach simulates an equivalent system were these properties are calculated to maximize the ratio between the lowest frequency, ω_0, and the maximum frequency, ω_{max}, $\frac{\omega_0}{\omega_{max}}$, which, as stated by Underwood [1983], maximizes the convergence rate to the steady state solution, by minimizing the spectral radius, ρ^*,

$$\rho^* = \left| 1 - 2\frac{\omega_0}{\omega_{max}} \right| \tag{56}$$

For this work, time step was chosen as the unity ($\Delta t = 1.0$) and, therefore, from Equation 51, one can obtain the equivalent mass and inertia of the scaled system.

$$1.0 = 2\sqrt{\frac{m_{scaled}}{k_{trans}}} \Leftrightarrow m_{scaled} = \left(\frac{1.0}{2} \right)^2 k^{trans} \tag{57}$$

$$1.0 = 2\sqrt{\frac{I_{scaled}}{k_{rot}}} \Leftrightarrow I_{scaled} = \left(\frac{1.0}{2} \right)^2 k^{rot} \tag{58}$$

The highest frequency, ω_{max}, is mesh and material dependent and the lowest frequency, ω_0, corresponds to the lowest participating mode of the structure, related to the load distribution [Tavarez and Plesha, 2007].

Sauvé and Metzger [1995] guarantee a level of tolerance for the stability of the algorithm by increasing the critical time step by a safety factor of 1.1% and obtaining the corresponding scaled mass and inertia (safety factor, SF).

Table 3.1 shows the model properties for the case of using real masses or scaled masses (density scaling).

Table 3.1 – Real and scaled system properties

Real properties	Properties using density scaling
m_{real}, I_{real}	$m_{scaled} = \left(\frac{1.0 \times SF}{2}\right)^2 k^{trans}$ *
	$I_{scaled} = \left(\frac{1.0 \times SF}{2}\right)^2 k^{rot}$
k^{trans}, k^{rot}	k^{trans}, k^{rot}
$\xi = \frac{c}{c_c}$	$\xi = \frac{c}{c_c}$
$c = c_c \xi$	$c = c_c \xi$
$c_c = 2\omega_0^{real} m_{real}$	$c_c = 2\omega_0^{scaled} m_{scaled}$
$\omega_0^{real} \approx$ {Equation 59}	$\omega_0^{scaled} \approx$ {Equation 59}
$\omega_{max}^{real} \approx$ {Equation 50}	
$\Delta t^{real} = 2\sqrt{\frac{m}{k}}$, (Equation 51)	$\Delta t^{scaled} = 1.0$

* where SF is a safety factor in order to guarantee convergence.

3.6 Adaptive dynamic relaxation

For damping the whole range of frequencies in an efficient way, a method, called dynamic relaxation (DR), is usually used [Underwood, 1983; Petrinic, 1996]. This method calculates an equivalent frequency, ω_0, through the Rayleigh's quotient. The advantage is that there is no need to determine the natural frequencies at each time step. This circular frequency, ω_0, is upper bounded by the maximum frequency, ω_{max}. Note that, when density scaling algorithm is adopted and time step is set to unity, $\omega_{max} < 2$ which results in $\omega_0 < \omega_{max} < 2$ [Azevedo, 2003; Underwood, 1983].

The goal of DR is to avoid overshooting the solution. For this an adaptive DR algorithm (ADR) is used in which the global damping coefficient, the mass and the inertia are updated at each time increment.

At each time step, the approximate fundamental frequency, ω_0, is recalculated using the diagonal matrix that approximates the global stiffness matrix, K^{diag} (non-assembled stiffness matrix).

An approximation of the lowest circular frequency, ω_0, associated to a loading condition is based on the principle of energy conservation, by the Rayleigh's quotient,

$$\omega_0^2 \approx \frac{u^T K u}{u^T M u} \tag{59}$$

where u^T and u are the current displacement vector and its transpose and K and M are the current tangent stiffness and mass matrix.

In this work, the adopted approach for the Rayleigh quotient is incremental based, using displacement increments, Δu^t [Underwood, 1983],

$$\omega_0^2 \approx \frac{\Delta u^T K^{diag} \Delta u}{\Delta u^T M \Delta u} \tag{60}$$

$$K_{ii}^{diag} = \frac{F_{i,t}^{int} - F_{i,t-\Delta t}^{int}}{u_{i,t} - u_{i,t-\Delta t}} \tag{61}$$

3.7 Convergence criteria

When converging to the steady state solution, a stopping criteria is needed to terminate the DR iterations.

Force and displacement tolerances, f_{tol} and u_{tol}, are defined for this convergence criteria. Within this work a tolerance of 0.001 was considered for the ratio between the mean of the unbalanced force norm, $\|F_t^{unbalanced}\|_{mean}$, and the mean contact force norm, $\|F_t^C\|_{mean}$, and for the ratio between the average displacement increment norm, $\|\Delta u_t\|_{mean}$, and the total displacement norm, $\|u_t\|_{mean}$, at a given time step,

$$\frac{\|F_t^{unbalanced}\|_{mean}}{\|F_t^C\|_{mean}} < f_{tol} \tag{62}$$

$$\frac{\|\Delta u_t\|_{mean}}{\|u_t\|_{mean}} < u_{tol} \tag{63}$$

3.8 Micro-macro approximations

3.8.1 Beam equivalence

The behaviour of a contact can be related to the behaviour of an equivalent beam and a general equivalence between contact micro properties, normal and shear stiffness, k_n and k_s, and material macro properties, elastic modulus, E.

The height of the equivalent beam, $\bar{R}$, is determined by the average radius of the particles, $R^{[A]}$ and $R^{[B]}$, and the beam length, L, is defined as the sum of both radius,

$$\bar{R} = \frac{R^{[A]} + R^{[B]}}{2} \tag{64}$$

$$L = 2\bar{R} = R^{[A]} + R^{[B]} \tag{65}$$

For 2D particle models, with t thickness, the equivalent cross-sectional area, A_{eq}, and moment of inertia, I_{eq}, is given by,

$$A_{eq} = 2.0\bar{R}t \tag{66}$$

$$I_{eq} = \frac{\left(2.0\bar{R}\right)^3 t}{12} \tag{67}$$

The equivalence between micro and macro properties follows,

$$k^n = \frac{EA}{L} \tag{68}$$

$$k^s = \frac{12EI}{L^3} \tag{69}$$

Which for pure axial load and pure shear load follows that,

$$k^n = k^s = Et \tag{70}$$

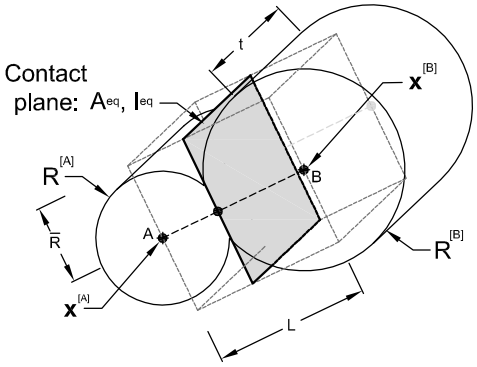

Figure 3.8 – Equivalent elastic beam

3.8.2 Elasticity theory

It is possible also to set an equivalence of elastic properties of a particle assembly to continuum elasticity theory, considering the Poisson's effect [Bolander and Saito, 1998],

$$k^n = \frac{E'h}{L}t \tag{71}$$

$$k^s = \frac{E''h}{L}t \tag{72}$$

$$E' = \frac{E}{1-\nu^2} \tag{73}$$

$$E'' = \frac{E}{2\left(1-\nu^2\right)} \tag{74}$$

where h is the contact height defined as the average diameter of both particles. This type of equivalence is used mostly for regular packing arrangements, where the relationship between micro and macro properties can be obtained directly from the former expressions. For random packing arrangements

it is usual set the equivalence to k_n and k_s using energy properties, for example, strain energy. This approximate values are then used as the first input parameters for the material calibration procedure.

3.8.3 Energy method

Assuming equal strain energy for the particle model and the equivalent beam the following expressions for the first estimate of the micro parameter values for the plane stress analysis has been proposed [Murat et al., 1992],

$$k_n = \frac{\sqrt{3}}{3\,(1-\nu)}E \tag{75}$$

$$k_s = \frac{\sqrt{3}\,(1-3\nu)}{3\,(1-\nu^2)}E \tag{76}$$

3.9 Contact constitutive models

3.9.1 Hooke's model

The elastic model is shown in Section 3.3 (Equations 11 and 12) as an incremental linear model, relating the incremental contact forces and the incremental relative displacement, for both normal and shear behaviours. Figure 3.9 illustrates the contact model properties for normal and shear behaviour, for both instantaneous and over time response. The normal and shear stiffness at contact interface is given by k_n and k_s, which do not change over time and yields a constant response over time for constant applied forces.

3.9.2 Burger's models

For this work, and to introduce time-dependent behaviour, the Burger's model was implemented. The Burger's model can be represented by a Kelvin and a Maxwell models placed in series and can be used to simulate creep and relaxation mechanisms in structural systems (E_M, η_M, E_K, η_K represent, respectively, the stiffness of the Maxwell unit, the viscosity of the Maxwell unit, the stiffness of the Kelvin unit and the viscosity of the Kelvin unit). Figure 3.10 shows the rheological model representing the Burger's model and the overlap response of the model for a constant contact force. The overlap response is divided into two parts: an elastic (instantaneous deformation) and a time-dependent deformation. The time-dependent deformation develops over time and has two parts, one from the viscosity of the Maxwell portion and another from the viscosity of the Kelvin portion.

The total Burger model displacement, U, is given by the sum of each component, the Maxwell model displacement (which is decomposed directly into two separate components, the spring displacement, U_{E_M}, and the dashpot displacement, U_{η_M}) and the Kelvin model displacement, U_K [Itasca Consulting Group Inc., 2008].

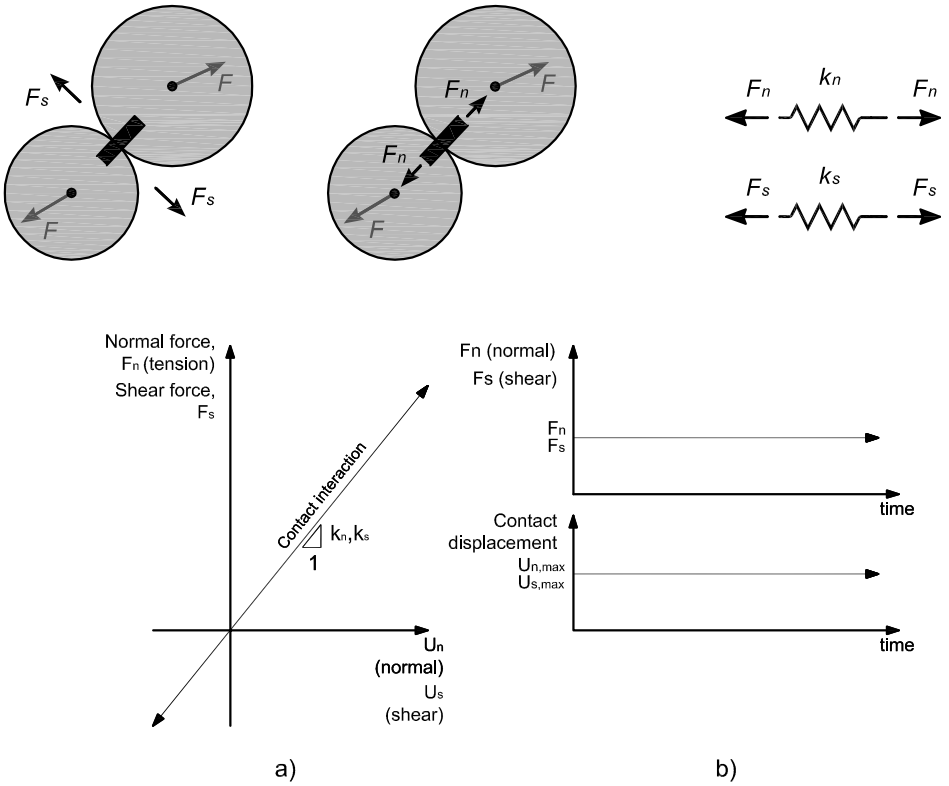

Figure 3.9 – Mechanical representation of the elastic model: a) Force-overlap diagram; b) Development of contact forces and overlap over time

$$U = U_{E_m} + U_{\eta_m} + U_K \tag{77}$$

Considering that applied forces are equal in the Maxwell and Kelvin models (placed in series), the force, F, at the Kelvin unit is obtained by Equation 78,

$$F = E_K U_K + \eta_K \dot{U}_K \tag{78}$$

For the Maxwell unit, the following constitutive relations can be drawn,

$$F = E_M U_{E_M} \tag{79}$$

$$F = \eta_M \dot{U}_{\eta_M} \tag{80}$$

Using the former relations, their derivatives and some mathematical manipulation, it is possible to obtain the differential equation that governs the Burger's model behaviour,

$$F + \left[\frac{\eta_K}{E_K} + \eta_M \left(\frac{1}{E_K} + \frac{1}{E_M}\right)\right] \dot{F} + \frac{\eta_K \eta_M}{E_K E_M} \ddot{F} = \eta_M \dot{U} + \frac{\eta_K \eta_M}{E_K} \ddot{U} \tag{81}$$

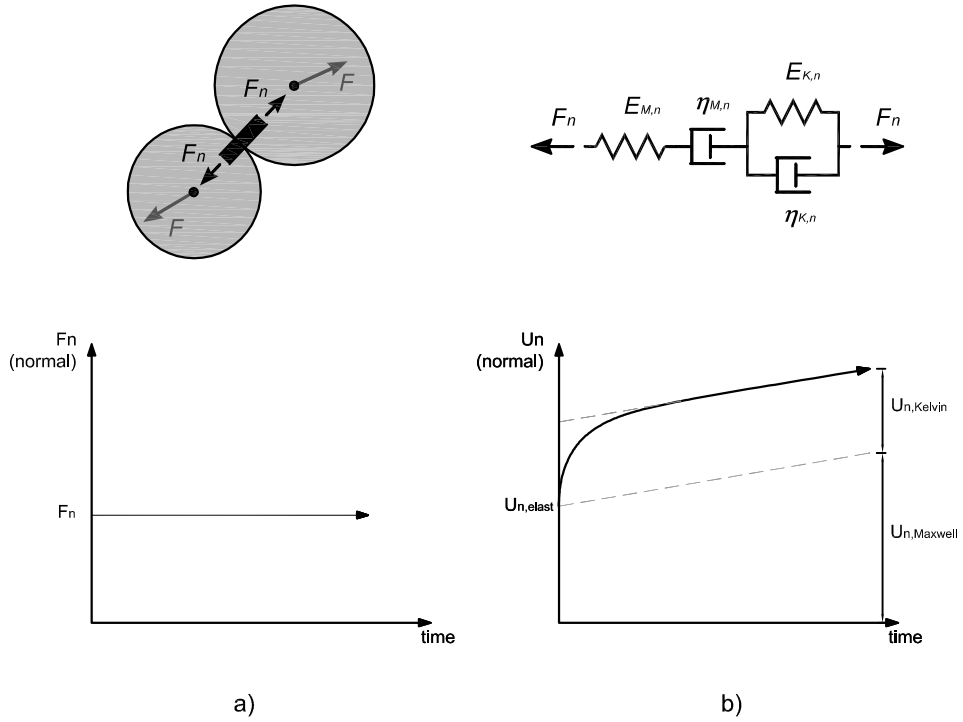

Figure 3.10 – Mechanical representation of the Burger model: a) Development of contact forces over time; b) Development of overlap over time

The analytical solution for the differential equation is obtained applying the Laplace transforms and their inverse [Findley et al., 1976].

For the creep behaviour of a constant applied force, $F(t) = F_0$, considering two initial conditions,

$$U(t=0) = \frac{F_0}{E_M} \tag{82}$$

$$\dot{U}(t=0) = \frac{F_0}{\eta_M} + \frac{F_0}{\eta_K} \tag{83}$$

the solution of the differential equation gives,

$$U(t) = \frac{F}{E_M} + \frac{F}{\eta_M}t + \frac{F}{E_K}\left(1 - e^{\left(-\frac{E_K}{\eta_K}t\right)}\right) \tag{84}$$

The relaxation behaviour of the Burger's model can be obtained considering an imposed displacement, U_0, at $t = 0$ [Findley et al., 1976],

$$U(t) = U_0 H(t) \tag{85}$$

$$\dot{U}(t) = U_0\delta(t), \quad \ddot{U}(t) = U_0\frac{\mathrm{d}\delta(t)}{\mathrm{d}t} \tag{86}$$

where $H(t)$ and $\delta(t)$ are the Heaviside and Dirac delta functions. The solution for these initial conditions yields,

$$F(t) = \frac{U_0}{A}\left[(q_1 - q_2 r_1)\, e^{-r_1 t} - (q_1 - q_2 r_2)\, e^{-r_2 t}\right] \tag{87}$$

where,

$$p_1 = \frac{\eta_M}{E_M} + \frac{\eta_M}{E_K} + \frac{\eta_K}{E_K}, \quad p_2 = \frac{\eta_M \eta_K}{E_M E_K} \tag{88}$$

$$q_1 = \eta_M, \quad q_2 = \frac{\eta_M \eta_K}{E_K} \tag{89}$$

$$A = \sqrt{p_1^2 - 4p_2} \tag{90}$$

$$r_1 = \frac{(p_1 - A)}{2p_2}, \quad r_2 = \frac{(p_1 + A)}{2p_2} \tag{91}$$

The adopted numerical scheme [Itasca Consulting Group Inc., 2008] relies on the central difference approximation using finite differences for the time derivatives of the Kelvin unit displacement, U_K, and the Maxwell unit displacement, U_M. From Equation (78), the first time derivative of U_K is given by

$$\dot{U}_K = \frac{-E_K U_K}{\eta_K} \tag{92}$$

which can be approximated by,

$$\dot{U}_K \approx \frac{U_K^{t+1} - U_K^t}{\Delta t} = \frac{1}{\eta_K}\left[-\frac{E_K\left(U_K^{t+1} + U_K^t\right)}{2} + \frac{F^{t+1} + F^t}{2}\right] \tag{93}$$

$$U_K^{t+1} = \frac{1}{A}\left[B U_K^t + \frac{\Delta t}{2\eta_K}\left(F^{t+1} + F^t\right)\right] \tag{94}$$

where,

$$A = 1 + \frac{E_K \Delta t}{2\eta_K}, \quad B = 1 - \frac{E_K \Delta t}{2\eta_K} \tag{95}$$

The total velocity of the Maxwell unit is given by the sum of the velocities of the Hooke's model and the

Newton model and, therefore, one can write,

$$\dot{U}_M = \frac{\dot{F}}{E_M} + \frac{F}{\eta_M} \tag{96}$$

which can be approximated by,

$$\dot{U}_M \approx \frac{U_M^{t+1} - U_M^t}{\Delta t} = \frac{F^{t+1} - F^t}{E_M \Delta t} + \frac{F^{t+1} - F^t}{2\eta_M} \tag{97}$$

$$U_M^{t+1} = \frac{F^{t+1} - F^t}{E_M} + \frac{\Delta t \left(F^{t+1} + F^t\right)}{2\eta_M} + U_M^t \tag{98}$$

As stated earlier, the total Burger's model displacement is given by the sum of the Kelvin and Maxwell models displacements, which can be approximated also by the finite difference scheme.

$$\Delta U = \Delta U_K + \Delta U_M \approx U^{t+1} - U^t = U_K^{t+1} - U_K^t + U_M^{t+1} - U_M^t \tag{99}$$

The contact force can be obtained from the former relations,

$$F^{t+1} = \frac{1}{C}\left[U^{t+1} - U^t + \left(1 - \frac{B}{A}\right) U_K^t - DF^t\right] \tag{100}$$

where,

$$C = \frac{\Delta t}{2\eta_K A} + \frac{1}{E_M} + \frac{\Delta t}{2\eta_M}, \quad D = \frac{\Delta t}{2\eta_K A} - \frac{1}{E_M} + \frac{\Delta t}{2\eta_M} \tag{101}$$

3.9.3 Delayed behaviour of concrete

For the definition of the delayed behaviour of concrete is usual to write the total strain, $\varepsilon(t, t')$, obtained from a applied stress at time t', $\sigma(t')$, as the sum of the instantaneous strains, $\varepsilon^i(t')$, the creep strains $\varepsilon^c(t, t')$, the shrinkage or dilatation strains, $\varepsilon^{sh}(t)$, and the thermal strains, $\varepsilon^T(t)$.

$$\varepsilon(t, t') = \varepsilon^i(t') + \varepsilon^c(t, t') + \varepsilon^{sh}(t) + \varepsilon^T(t) \tag{102}$$

Considering from here on only the stress-dependent strain, $\varepsilon_\sigma(t, t') = \varepsilon^i(t') + \varepsilon^c(t, t')$, as a function of stress, $\sigma(t')$, we obtain a constitutive relation (Equation 103), in which $J(t, t')$ is the creep compliance (strain at the time t due to a unit stress applied at time t'). The remaining terms of Equation 102 constitute the stress-independent strain, defined by $\varepsilon^0(t) = \varepsilon^{sh}(t) + \varepsilon^T(t)$.

$$\varepsilon(t, t') = J(t, t')\sigma(t') \tag{103}$$

The same constitutive equation in terms of strain history can be written as,

$$\sigma(t) = R(t,t')\varepsilon(t') \tag{104}$$

where $R(t,t')$ is the relaxation function (stress at time t due to a unit strain applied at time t').

Creep compliance can be written as a sum of unit instantaneous deformation ($1/E(t')$) and specific creep deformation ($C(t,t')$),

$$J(t,t') = \frac{1}{E(t')} + C(t,t') \tag{105}$$

Although the instantaneous behaviour of concrete is a fictitious concept, it is usual to separate instantaneous and specific creep strains. Instantaneous deformation value is, actually, a function of loading rate and, therefore, constitutes a part of the total deformation. Because several test results are considered "instantaneous" is necessary to define were does instantaneous strains ends and creep strains start. To overcome this particular aspect is common to define instantaneous strain as the compliance values for a small loading time, Δt (Equation 106).

$$\frac{1}{E(t')} = J(t' + \Delta t, t') \tag{106}$$

Concrete can be considered as a time-dependent linear viscoelastic material provided that stress is less than 0.4 of the compression strength and that large sign inversion, large cyclic strains or even significant changes in water content and temperature do not occur [Bažant and Wu, 1973]. As a consequence of this hypothesis, we can use the principle of superposition given by the Stieltjes integral,

$$\varepsilon(t,t') - \varepsilon^0(t) = \varepsilon_\sigma(t,t') = \int_0^t J(t,t')\frac{\mathrm{d}\sigma(t')}{\mathrm{d}t'}\mathrm{d}t' = \int_0^t J(t,t')\mathrm{d}\sigma(t') \tag{107}$$

Since concrete's microstructure is always in development, due to hydration of silicates and aging, is not possible to apply classical viscoelasticity to interpret its behaviour and it is necessary to implement step-by-step time integration methods [Bažant and Wu, 1973].

3.9.4 Solidification theory

According to the solidification theory proposed by Bažant and Prasannan [Bažant, 1988], aging is due to cement hydration (formation of new calcium hydrates) and, probably, due to gradual formation of bonds as a result of polymerization. This complicates concrete numerical modelling because:

- Rheological models, with time-dependent moduli and viscosities, are difficult to deal with;
- Time-dependent parameters are difficult to calibrate from test data;
- Thermodynamic restrictions are difficult to formulate.

The main idea of solidification theory is to treat aging as a "consequence of volume growth of the load-bearing solidified matter (hydrated cement) whose properties are non-aging and are described by a Kelvin chain with age-independent moduli and viscosities" [Bažant, 1988].

As seen before and as shown in Figure 3.11, the total strain can be divided into three parts,

$$\varepsilon = \frac{\sigma}{E_0} + \varepsilon^c + \varepsilon^0 \tag{108}$$

where ε^c is the creep strain, composed by ε^v, viscoelastic strain, and ε^f, viscous strain,

$$\varepsilon^c = \varepsilon^v + \varepsilon^f \tag{109}$$

and σ is the applied stress, E_0 is the elastic modulus and ε^0 is the sum of hygrothermal strain (drying shrinkage, thermal dilatation, chemical strain or autogeneous shrinkage and, for high stresses, cracking strain).

For high stresses, the dependence of ε^v and ε^f on stress becomes nonlinear and represent viscoelastic-plastic strain and viscoplastic strain, respectively.

The elastic part σ/E_0 is the deformation of the mineral aggregate pieces and the microscopic elastic particles of hardened cement paste (anhydrous cement grains + calcium hydroxide crystals + crystalline particles in cement gel). Chemically the elastic properties of all components are constant. Despite that it is usual to consider the elastic strain as a function of age, $\sigma/E(t)$, Bažant considers this to be a complication and thermodynamically invalid. Therefore, suggests using E_0 as a material constant, defined as the asymptotic modulus, a modulus applicable to very short-load durations (below 1 μ second). The measured elastic strain is only an apparent elastic strain which is age-dependent and represents the sum of the elastic part σ/E_0 and short-time creep (for loading durations of 1 minute to 1 hour). This concept was already used in double power law [Bažant and Osman, 1976], log-double power law [Bažant and Chern, 1985a] and triple power law [Bažant and Chern, 1985b].

The proposed model, based on the solidification theory, considers the viscoelastic strain, ε^v, a consequence of the volume fraction growth, $v(t)$, and the viscous strain, ε^f, a consequence of the volume fraction growth, $h(t)$, and are mathematically formulated in [Bažant, 1977] and [Bažant and Prasannan, 1989a] (Figure 3.11).

The concept of the viscoelastic part is that each increment of $v(t)$, $dv(t)$, represents a deposited layer on the surface of the solidified material. The increment volume, $dv(t)$, is subjected to the same strain, $\varepsilon^v(t)$, which results in a parallel coupling of all the increment volumes.

For the mathematical formulation, Bažant introduces the concept of microstress, $\sigma_g(v,t)$, in the solidified matter (cement gel) at time t (Figure 3.11). A layer of thickness, $dv(\tau)$, is assumed to solidify and bearing with the previously solidified matter at time τ. The sum of all the microstress since $t = 0$ is the total macroscopic stress,

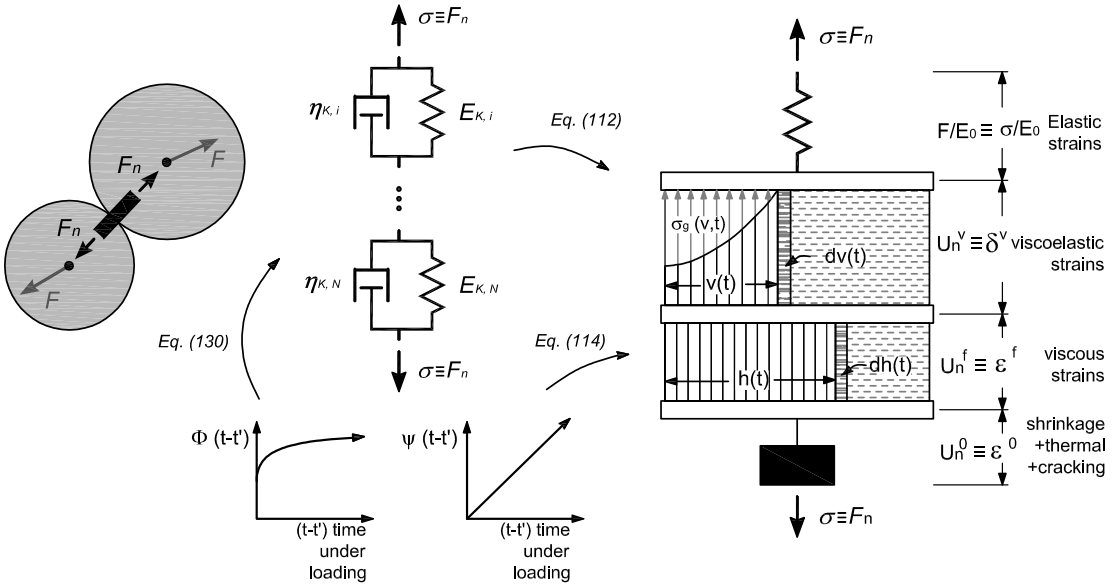

Figure 3.11 – Solidification theory based on Kelvin chain model

$$\sigma(t) = \int_{\tau=0}^{t} \sigma_g \left[v(\tau), t\right] dv(\tau) \tag{110}$$

Considering that the solidifying material on the microscale is a non-aging and linearly viscoelastic material, the macroscopic stress-strain relationship is given by,

$$\varepsilon^v(t) - \varepsilon^v(\tau) = \int_0^t \Phi(t-t')\sigma_g \left[v(\tau), t'\right] \tag{111}$$

where,

- $\sigma_g \left[v(\tau), t'\right] = 0$ for $t' < \tau$
- $\varepsilon^v(t) - \varepsilon^v(\tau)$ is the viscoelatic strain
- $\Phi(t-t')$ is the microscopic creep compliance function.

The simplification is that $\Phi(t-t')$ is a function of only one variable $(t-t')$, the loading duration, instead of two variables (loading duration and age), as stated in previous formulations for the delayed behaviour of concrete, described, for example, in [Bažant and Osman, 1976]. The Kelvin chain model shown in Figure 3.11 represents the non-aging viscoelastic strains.

It is known that the creep curves change with increasing age for as long as 10 year (aging) and that the development of new hydrates terminates much earlier. Therefore, is not possible to say that the evolution of $v(t)$ is only related to hydration. There are evidence that $v(t)$ fraction continues to grow after maximum hydration is reached as a consequence of the increase of bonds between solid matter (polymerization).

It is important to point out that each layer $dv(\tau)$ solidifies at a free state stress, $\sigma_g\left[v(\tau),\tau\right]=0$. The constitutive relations can be simplified when considering this hypothesis [Bažant, 1977],

$$\dot{\varepsilon}^v(t)=\frac{1}{v(t)}\dot{\gamma}(t)=\frac{1}{v(t)}\int_0^t\dot{\Phi}(t-t')d\sigma(t') \tag{112}$$

where $\dot{\Phi}(t-t')=d\Phi(t-t')/dt$ and $v(t)$ can is taken as a function of time and of empirical variables λ_0, m and α,

$$\frac{1}{v(t)}=\left(\frac{\lambda_0}{t}\right)^m+\alpha \tag{113}$$

and the variable $\gamma(t)$ can be seen as the viscoelastic microstrain of the growing volume.

The second part of the creep strains is related to the viscous flow and its derivative can be represented by,

$$\dot{\varepsilon}^f(t)=\frac{\sigma(t)}{\eta(t)}=\frac{\sigma(t)}{h(t)}\int_0^t\dot{\Psi}(t-t')d\sigma(t') \tag{114}$$

where $\Psi(t-t')$ is the microscopic compliance viscous function of the solidified matter (non-aging), $\eta(t)=\eta_0 h(t)$ is the apparent macroscopic viscosity given by $\eta(t)=t/q_4$ (Figure 3.11).

Therefore, when considering constant stress, $\sigma(t')$, one can write,

$$\dot{\varepsilon}(t)=\sigma\dot{C}(t,t')+\dot{\varepsilon}^0 \tag{115}$$

$$\dot{C}(t,t')=\frac{\Phi(t-t')}{v(t)}+\frac{1}{\eta(t)} \tag{116}$$

$$J(t,t')=\frac{1}{E_0}+\int_0^t\dot{C}(t,t')d\tau=\frac{1}{E_0}+\left(\frac{\Phi(t-t')}{v(t)}+\frac{1}{\eta(t)}\right)d\tau \tag{117}$$

where $\dot{C}(t,t')$ is the creep compliance rate and $J(t,t')$ is the creep compliance function.

The compliance rate can be written as a function of the material parameters

$$\dot{C}(t,t')=\frac{\partial J(t,t')}{\partial t}=\left[q_2\left(\frac{\lambda_0}{t}\right)^m+q_3\right]\frac{n\xi^{n-1}}{\lambda_0(1+\xi^n)+\frac{q_4}{t}} \tag{118}$$

where $q_3=\alpha q_2$. The creep compliance, considering the initial value of $\varepsilon(t,t')=\sigma/E_0$, is,

$$J(t,t')=q_1+q_2Q(t,t')+q_3ln\left[1+\left(\frac{t-t'}{\lambda_0}\right)^n\right]+q_4ln\left(\frac{t}{t'}\right) \tag{119}$$

where $J(t,t')=\varepsilon(t,t')/\sigma(t')$, $q_1=1/E_0$ and,

$$Q(t,t') = \int_{t'}^{t} \left(\frac{\lambda_0}{\tau}\right)^m \frac{n(\tau - t')^{n-1}}{\lambda_0^n (1 + \tau - t')^n} d\tau \tag{120}$$

Derived from solidification theory and proposed by Bažant and Baweja [Bažant and Baweja, 1995, 2000], $J(t,t')$ can be described as the sum of q_1, the elastic instantaneous strains due to unit stress, $C_0(t,t')$, the basic creep complaince and $C_d(t,t',t_0)$, the drying creep compliance (Equation 121). For this work, drying creep strains are not considered (t_0 is the age of drying).

$$J(t,t') = q_1 + C_0(t,t') + C_d(t,t',t_0) \tag{121}$$

Basic creep compliance, $C_0(t,t')$ in Equation 122, can be expressed as a linear combination of parameters and time-dependent variables [Bažant and Prasannan, 1989b]: the first part is responsible for the aging viscoelastic compliance, the second for the non-aging viscoelastic compliance and the last one for the flow compliance. It is usual to consider, for all types of concrete, $n = 0.1$, $m = 0.5$ and $\lambda = 1\ day$.

$$C_0(t,t') = q_2\, Q(t,t') + q_3\, \ln\left[1 + (t - t')^n\right] + q_4\, \ln\left(\frac{t}{t'}\right) \tag{122}$$

where $Q(t,t')$ is a binomial integral (Equation 120) with no analytical expression but can be approximated by Equation 123,

$$Q(t,t') = Q_f(t') \left[1 + \left(\frac{Q_f\left(t'\right)}{Z\left(t,t'\right)}\right)^{r(t')}\right]^{-1/r(t')} \tag{123}$$

where,

$$r\left(t'\right) = 1.7\, \left(t'\right)^{0.12} + 8 \tag{124}$$

$$Z\left(t,t'\right) = \left(t'\right)^{-m}\, \ln\left[1 + \left(t - t'\right)^n\right] \tag{125}$$

$$Q_f\left(t'\right) = \left[0.086\, \left(t'\right)^{2/9} + 1.21\, \left(t'\right)^{4/9}\right]^{-1} \tag{126}$$

The approximation error is less than 1% for $n = 0.1$ and $m = 0.5$ [Bažant and Baweja, 2000]. The model parameters, q_1, q_2, q_3 and q_4 can be obtained from linear regression fit to test results.

The static modulus of elasticity, for comparison with test results at a given age, can be calculated from Equation 127, considering a stress duration, $\Delta = t - t' = 0.01$ days,

$$E(t') = \frac{1}{A_0 + \frac{A_1}{\sqrt{t'}}} \tag{127}$$

where $A_0 = q_1 + q_3 ln(1 + \Delta^n)$ and $A_1 = q_2 ln(1 + \Delta^n)$.

3.9.5 Numerical formulation of solidification theory

Despite the integral nature of the creep analysis (Equation 107), it is possible to find an equivalence between the integral-type creep law and a rate-type form.

Considering the solidification theory, the rheological model of the solidified matter is taken as a non-aging Kelvin chain, where the viscoelastic microstrain, $\gamma(t)$, is given by the sum of each Kelvin unit,

$$E_\mu \gamma_\mu + \eta_\mu \dot{\gamma}_\mu = \sigma, \quad \gamma = \sum_\mu^N \gamma_\mu \tag{128}$$

$$\gamma(t) = \sigma \sum_\mu^N \frac{1}{E_\mu} \left(1 - e^{-(t-t'/\tau_\mu)}\right), \quad \tau_\mu = \frac{\eta_\mu}{E_\mu} \tag{129}$$

In the above equations, τ_μ , E_μ and η_μ are the retardation time, the modulus of elasticity and the viscosity coefficient of the μ Kelvin unit.

Similarly, the microscopic creep compliance function, $\Phi(t-t')$, can be approximated by a Dirichlet series,

$$\Phi(t - t') = A_0 + \sum_\mu^N A_\mu \left(1 - e^{-(t-t'/\tau_\mu)}\right) \tag{130}$$

Bažant and Xi [1995] recommend the use of the continuous retardation spectra, $L(\tau_\mu)$, and a logarithmic discretization of retardation times for the determination of the A_μ coefficients,

$$\tau_2 = 0.5, \tau_1 = 1 \times 10^{-5} \tau_2, \quad \tau_\mu = 10\tau_{\mu-1}, \quad \mu = 3, 4, \cdots \tag{131}$$

$$A_\mu = L(\tau_\mu)\Delta(ln(\tau_\mu)) = L(\tau_\mu) ln10 \tag{132}$$

$$\begin{aligned} L(\tau_\mu) = &\left[\frac{-2n^2(3\tau)^{2n-3}[n-1-(3\tau)^n]}{[1+(3\tau)^n]^3}\right]\frac{(3\tau)^3}{2}q_2 + \\ &+ \left[\frac{n(n-2)(3\tau)^{n-3}[n-1-(3\tau)^n] - n^2(3\tau)^{2n-3}}{[1+(3\tau)^n]^2}\right]\frac{(3\tau)^3}{2}q_2 \end{aligned} \tag{133}$$

Bažant et al. [2004] determine the coefficient A_0 from the remaining area of the spectra not represented by the chosen retardation times (for $\tau < \tau_1$),

$$A_0 = \frac{1}{\xi_N}\int_0^{\xi_N}\left\{\Phi(\xi) - \sum_{\mu}^{N} A_\mu\left(1 - e^{-\xi/\tau_\mu}\right)\right\}d\xi \tag{134}$$

where ξ_N is maximum retardation time and under the solidification theory hypothesis of the $\Phi(t-t') = q_2 ln\,(1+\xi^n)$, $\xi = (t-t')/\lambda_0$ and $\lambda_0 = 1.0$. The coefficients for the viscoelastic microstrains, E_μ, are obtained by $E_\mu = A_\mu/q_2$.

Considering that the stress varies linearly between a given time step (t_i, t_{i+1}), $\sigma(t) = \sigma_i + \Delta\sigma$, the component of each Kelvin unit can be calculated from,

$$\gamma_{\mu,i+1} = \gamma_{\mu,i}e^{-\Delta y_\mu} + \frac{\sigma_i}{E_\mu}(1 - e^{-\Delta y_\mu}) + \frac{1-\lambda_\mu}{E_\mu}\Delta\sigma, \quad \Delta y_\mu = \frac{\Delta t}{\tau_\mu}, \quad \lambda_\mu = \frac{1 - e^{-\Delta y_\mu}}{\Delta y_\mu} \tag{135}$$

The total increment of viscoelastic microstrain, $\Delta\gamma$, can be obtained from the sum of each Kelvin unit, $\Delta\gamma = \sum_{\mu=1}^{N}(\gamma_{i+1} - \gamma_i)$ and an incremental form can be written,

$$\Delta\gamma = \sum_{\mu=1}^{N}\left(\frac{1-\lambda_\mu}{E_\mu}\right)\Delta\sigma + \Delta\gamma'' \tag{136}$$

$$\Delta\gamma'' = \sum_{\mu=1}^{N}\Delta\gamma''_\mu = \sum_{\mu=1}^{N}\left(\frac{\sigma_i}{E_\mu} - \gamma_{\mu,i}\right)\left(1 - e^{-\Delta\gamma_\mu}\right) \tag{137}$$

The total increment of viscoelastic strain, $\Delta\varepsilon^v$, is given by Equation 112,

$$\dot{\varepsilon}^v(t) = \frac{1}{v(t)}\dot{\gamma}(t) \backsim \Delta\varepsilon^v = \frac{1}{v(t^*)}\Delta\gamma = \frac{1}{v(t^*)}\left[\sum_{\mu=1}^{N}\left(\frac{1-\lambda_\mu}{E_\mu}\right)\Delta\sigma + \Delta\gamma''\right] \tag{138}$$

where $t^* = t_0 + [(t_{i+1} - t_0)(t_i - t_0)^{1/2}]$ which represents the middle of the time step in the logarithmic time scale.

Taking into account the flow strain increment, $\Delta\varepsilon^f = q_4\sigma\Delta t/t^*$, and the increment of instantaneous elastic strain, $q_1\Delta\sigma$, one can write the full incremental quasi-elastic stress-strain relation,

$$\Delta\varepsilon = \frac{\Delta\sigma}{E''} + \Delta\varepsilon'' \tag{139}$$

where,

$$\frac{1}{E''} = q_1 + \frac{A_0}{v(t^*)} + \frac{1}{v(t^*)}\sum_{\mu=1}^{N}\left(\frac{1-\lambda_\mu}{E_\mu}\right) \tag{140}$$

$$\Delta\varepsilon'' = \frac{\Delta\gamma''}{v(t^*)} + \frac{q_4\sigma(t^*)\Delta t}{t^*} \tag{141}$$

3.10 Numerical incremental scheme for fast simulation of creep behaviour using DEM

3.10.1 General procedures

The numerical stability of explicit integration schemes rely on a maximum time step value that can be very small. To simulate the creep behaviour of structural systems, such as rock or concrete, the total calculation time can be expensive. Feng et al. [2003] proposed a numerical scheme for overcoming the need of a large number of steps based on the introduction of incremental contact forces equivalent to the expected creep deformation. This scheme make use of both the dynamic relaxation procedure to obtain a fast equilibrium without overshooting and of the viscoelastic contact model (although indirectly).

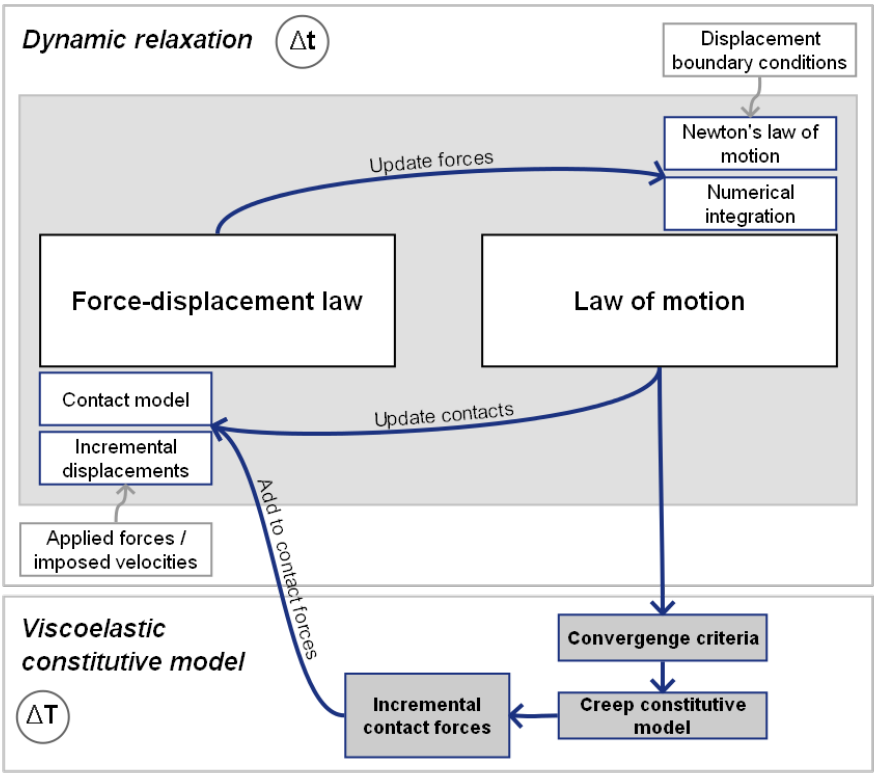

Figure 3.12 – General DEM cycle with incremental creep constitutive model [Feng et al., 2003]

The procedure is divided into two main parts shown in Figure 3.12: *dynamic relaxation,* Δt, for converging to the solution by dynamic relaxation, using a time increment, Δt (similar to the procedure defined earlier in §3.1); and *viscoelastic constitutive model* ΔT for large time increments, ΔT, for setting the incremental contact force obtained from the creep constitutive model (introduced into the code after each dynamic relaxation convergence).

Considering the increment of viscoelatic displacement, ΔU_{visco}, one can consider an equivalent incremental contact force, which can be added to the contact forces in the model and introducing an unbalanced state, which is set to equilibrium through dynamic relaxation, using the time increment, Δt.

Once the equilibrium is obtained for the time step, T_{i+1}, a new time increment is imposed, ΔT, the new incremental viscoelastic displacement, ΔU_{visco}, is calculated and the incremental contact forces, ΔF_c, is again added into each contact.

3.10.2 Burger model

Considering a constant applied force, $F(t) = F_0$, the viscoelastic part of the Burger's model at a given time, T_i, is given by,

$$U_{visco}(T) = \frac{F_0}{\eta_M} T_i + \frac{F_0}{E_K} \left(1 - e^{\left(-\frac{E_K}{\eta_K} T_i\right)}\right) \tag{142}$$

For a given time increment, $\Delta T = T_{i+1} - T_i$, the increase of viscoelastic displacement is,

$$\Delta U_{visco}(T) = \frac{F_0}{\eta_M} \Delta T + \frac{F_0}{E_K} \left(e^{\left(-\frac{E_K}{\eta_K} T_i\right)} - e^{\left(-\frac{E_K}{\eta_K} T_{i+1}\right)}\right) \tag{143}$$

$$\Delta F_c(T_{i+1}) = -E_M \Delta U_{visco}(T) \tag{144}$$

$$F_c(T_{i+1}) = F_c(T_i) + \Delta F_c(T_{i+1}) \tag{145}$$

3.10.3 Solidification theory

Considering a constant applied force, $F(T = 0) = F_0$, for a given time increment, $\Delta T = T_{i+1} - T_i$, the increase of viscoelastic strain for the solidification theory is given by the incremental quasi-elastic stress-strain relation (Equations 139, 140 and 141) and, therefore, the incremental contact forces, ΔF_c are obtained from

$$\Delta \varepsilon(T_i) = \Delta \varepsilon''(T_i) \equiv \Delta U_{visco}(T_i) = \Delta U''(T_i) \tag{146}$$

$$\Delta \sigma(T_{i+1}) = \varepsilon''(T_i) E''(T_i) \equiv \Delta F_c(T_{i+1}) = \Delta U_{visco}(T_i) E''(T_i) \tag{147}$$

$$F_c(T_{i+1}) = F_c(T_i) + \Delta F_c(T_{i+1}) \tag{148}$$

The first displacement increment, $U_{elastic}(T = 0)$, is given by a dynamic relaxation procedure considering elastic behaviour and the modulus of elasticity at the age of loading, given by Equation 127.

3.11 C++ code implementation for elastic and viscoelastic behaviour

For the implementation of the DEM, the former concepts and procedures were structured into a C++ computational code [Microsoft Corporation, 2010]. Figure 3.13 shows a schematic view of the code's structure, divided into three main parts. The first SETUP part deals with the definition of properties, geometries, boundary and analysis conditions. It is possible to generate a regular, rectangular or hexagonal, mesh, and to built input data files for a generic mesh (including several types of materials). The second part, CYCLE, iterates over time and applies the law of motion and the law of forces to all the particles and contacts until the convergence criteria is reached and the third part, OUTPUT, is where the main results are written into ASCII files, including data files (.dad) and files with the undeformed and deformed meshs (using .vtk files).

The complete algorithm is summarized in the following steps:

SETUP

1. Generation of particle assembly (predefined mesh, rectangular or hexagonal, or user-defined mesh);
2. Definition of contacts;
3. Definition of boundary and loading conditions;
4. Definition of real or scaled masses;
5. Calculation of the critical time step or the scaled masses;
6. Definition of the stopping criteria (maximum simulation time, maximum number of steps and convergence criteria using force and displacement tolerances);
7. Set type of damping;
8. Set constitutive law;
9. Calculation of analytical frequency, ω_{analyt}, for global damping;
10. Calculation of the initial velocities and positions (obtained from an undamped system);

CYCLE

11. Law of motion:
    (a) Calculation of new velocities;
    (b) Calculation of new positions;
    (c) Calculation of displacements;
    (d) Update of the velocities and positions.
12. Law of forces:

(a) Calculation of overlap;

(b) Calculation of contact position;

(c) Calculation of contact velocity;

(d) Calculation of incremental contact displacement;

(e) Calculation of incremental contact forces;

(f) Calculation of total contact forces;

(g) Calculation of total particle forces;

(h) Updates of the total particle forces.

13. Recalculation of critical time step or scaled masses;

14. Recalculation of natural frequency, ω_0;

15. Check convergence criteria (unbalanced force or displacement criteria). If convergence is reached, exit; otherwise, go to 11.

OUTPUT

The output files are composed by ".dad" file types with the results obtained for the control particles, including particle ID, step, time, particle position, particle velocity and particle forces, a ".info" file with the information about the analysis and ".vtk" files for the graphical representation of the system.

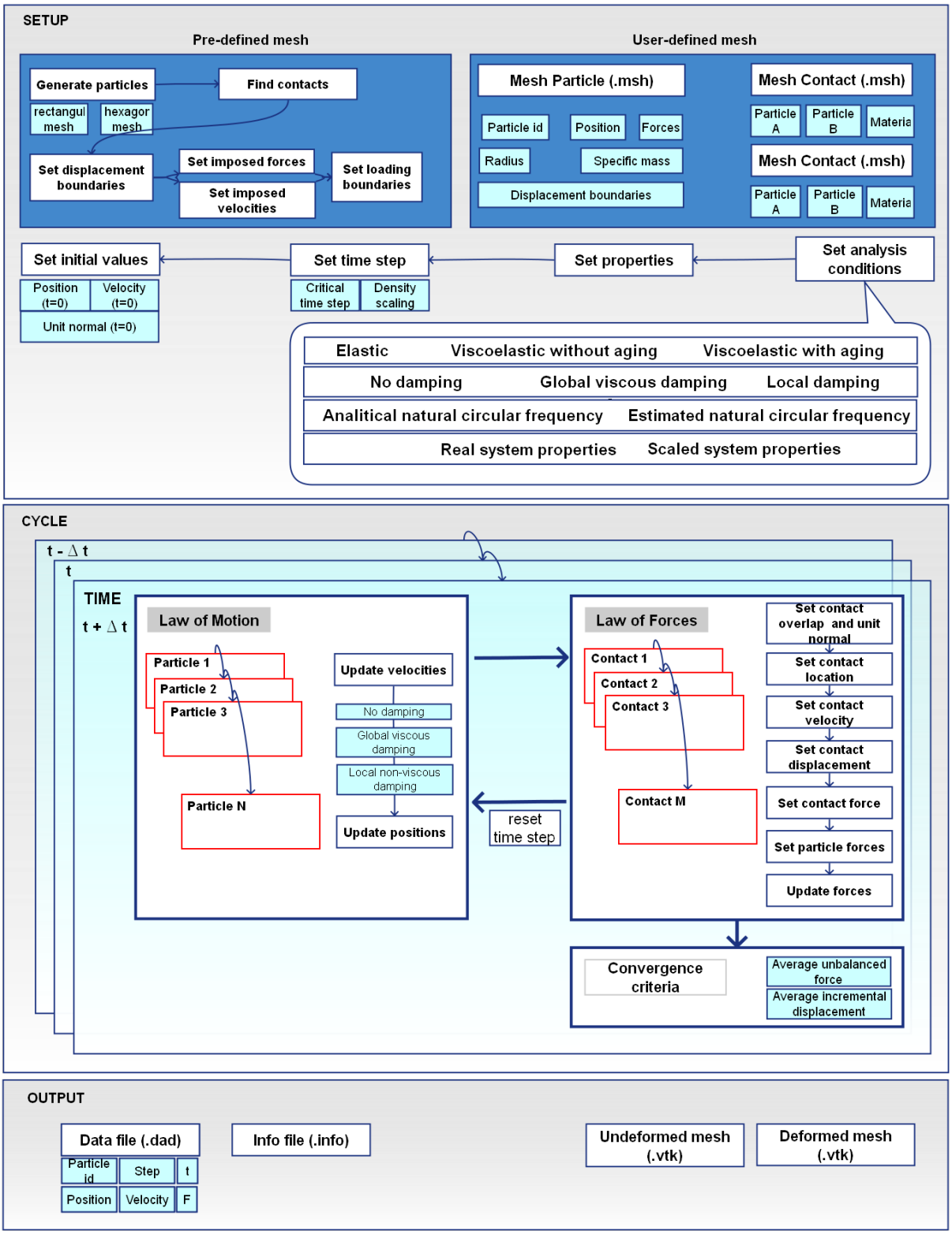

Figure 3.13 – C++ discrete element method code flowchart

Figure 3.14 shows the structure used for the code implementation using C++. The definition of classes "Particle" and "Contact" within the "Domain" allows for the use of object-oriented programming and for each problem "Particle" and "Contact" objects are created were their properties and specific "functions" are predefined.

The Particle.cls class file includes the properties regarding the rigid particles, such as the radius, the specific mass, the position ()displacements and rotations) the linear velocities and angular velocities and defines functions to deal with those properties. The Contact.cls class file defines the properties and functions related to the interaction of two particles, such as the ID of particle A and particle B, the contact normal and shear stiffness.

The global functions are defined in the Domain.cls class file which controls the SETUP, CYCLE and OUTPUT phases. In the CYCLE phase, the domain class calls the law of motion and the law of forces functions for each time step until the convergence criteria is reached.

In the OUTPUT phase the main results for a set of particles ($ID = N$) and contacts ($ID = M$) are written into ASCII files (..._part_ID_N.dad and ..._cont_ID_M.dad). The results are also written in .vtk format for the representation into a graphical view using, for example, the ParaView software [Ayachit, 2005].

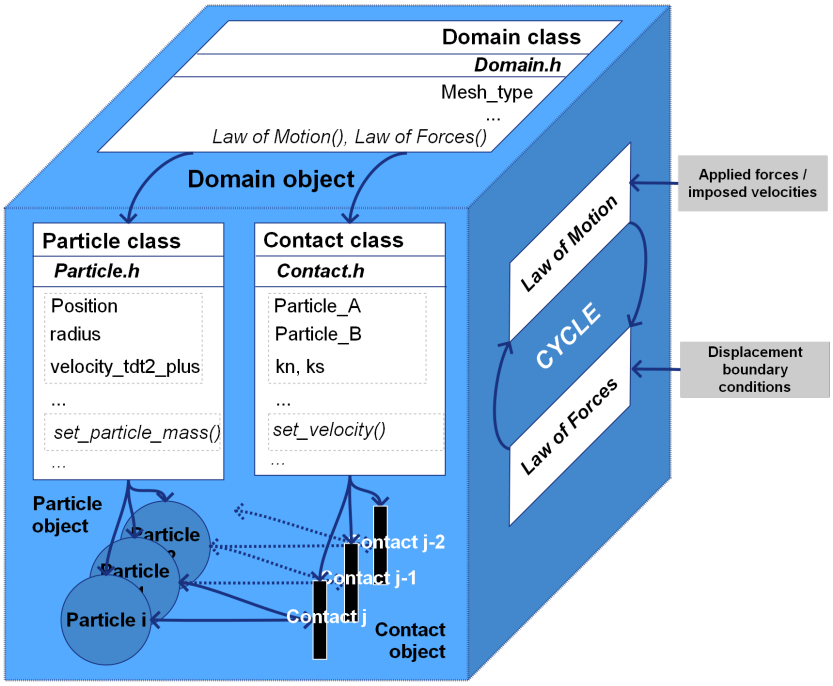

Figure 3.14 – C++ classes

3.12 C++ code implementation of numerical incremental scheme for fast simulation of creep behaviour

The complete algorithm is summarized in the following steps:

1. Generation of particle assembly (rectangular or hexagonal);
2. Definition of contacts;
3. Definition of boundary and loading conditions;
4. Definition of real or scaled masses;
5. Calculation of the critical time step or the scaled masses;
6. Definition of the stopping criteria (maximum simulation time or maximum number of steps);
7. Set type of damping;
8. Set constitutive law;
9. Calculation of the initial velocities and positions (obtained from an undamped system);
10. Start the cycle for time-dependent behaviour:
    (a) Setting creep time, $T_i = 0$, creep time increment, ΔT and maximum creep time of analysis, T_{max}:
    (b) Starting the cycle for dynamic relaxation, considering DR time, t and a DR time step, Δt:
        i. Law of motion:
        ii. Law of forces:
        iii. Recalculation of critical time step or scaled masses;
        iv. Recalculation of natural frequency, ω_0;
        v. Checking convergence criteria (unbalanced force or displacement criteria). If convergence is reached, exit. Otherwise, go to i).
    (c) Increase of time to T_{i+1}. If $T_{i+1} \geq T_{max}$, exit. Otherwise, return to b).
    (d) Calculation of viscoelastic displacement increment, ΔU_{visco}, for T_{i+1};
    (e) Calculation of incremental contact force, ΔF_c, add to the contact force, F_c;

4| Verification of code implementation

4.1 Testing models

The code verification was made by testing the behaviour of three types of geometries with different types of loadings, varied analysis conditions and implemented constitutive models: elastic (Hooke's model), viscoelastic (Burger's model) and viscoelastic with aging (solidification theory).

The following section shows the results from the three geometries and loading conditions, for both elastic and viscoelastic behaviour, namely:

1. Two particles (2×1) in pure tension (Figure 4.16);
2. Four particles (2×2) in shear (Figure 4.25);
3. Cantilever beam test with 20×5 particles in bending (Figure 4.32).

For the elastic model and for each geometry, several analysis were made in order to test the implementation, namely with:

1. No damping;
2. Global viscous damping, with analytical estimate of ω_0, using:
   (a) Critical time step;
   (b) Density scaling.
3. Adaptive dynamic relaxation (ADR), using:
   (a) Critical time step;
   (b) Density scaling.
4. Local non-viscous damping, using:
   (a) Critical time step;
   (b) Density scaling.

Finally, the verification of the models is also obtained considering the three type of macro-micro approximation, defined previously in Section 3.8. For the Burger's model and for each geometry, several analysis were made in order to test the implementation, namely, with:

1. No damping;
2. Adaptive dynamic relaxation (ADR):

For the aging model based on the solidification theory, two predefined meshs (2×1 particles and 20×5 particles) were tested in order to reproduce the concrete test results of Rostasy et. al. from 1971 [Bažant and Prasannan, 1989a]:

1. Adaptive dynamic relaxation (ADR):

   (a) Critical time step.

For testing the numerical incremental scheme for fast behaviour simulation using DEM (§3.10), the two delayed models were used, Burger's model and aging model, for both normal and shear loadings (2×1 particles and 20×5 particles). These examples combine the incremental scheme for predefined large time steps (ΔT) and an adaptive dynamic relaxation (ADR) using the critical time step (Δt) for obtaining the equilibrium at each time, T_i.

4.2 Elastic behaviour - Hooke's model

4.2.1 Model properties

For the static elastic behaviour (Hooke's model) the considered properties are presented in Table 4.2.

Table 4.2 – Mechanical properties of Hooke's model testing examples

radius	**specific mass**	k_n	k_s	F	v
$[m]$	$[ton/m^3]$	$[kN/m]$	$[kN/m]$	$[kN]$	$[m/s]$
50.0	1000	1.35×10^9	1.35×10^9	100	1×10^{-5}

The dynamic properties of the test models, the natural frequencies, ω_i, can be obtained from the analytical solution of longitudinal and transverse vibrations of continuous bars [Clough and Penzien, 1993].

For longitudinal vibrations, considering $u(x,t)$ the displacements in the longitudinal direction of a bar with modulus of elasticity, E, and cross-section, A, one can separate the harmonic time variation $Y(t)$ and the deformed shape $\phi(x)$ representing the behaviour ($u(x,t) = \phi(x)Y(t)$. The differential equation of motion of $u(x,t)$ does not depend on $Y(t)$,

$$\ddot{\phi}(x) + \left(\frac{\omega}{c_0}\right)^2 \phi(x) = 0, \quad c_0 = \sqrt{\frac{EA}{m}} \tag{149}$$

and solution for $\phi(x)$ is,

$$\phi(x) = A \sin\left(\frac{\omega}{c_0}x\right) + B \cos\left(\frac{\omega}{c_0}x\right) \tag{150}$$

where ω is the circular frequency of the system for time-dependent behaviour, $Y(t)$.

For a cantilever bar with L length, fixed at one end and free in another, one have $\phi(x = 0) = 0$ and $\ddot{\phi}(x = 0) = 0$ as boundary conditions and the following natural frequencies, ω_i, are obtained from,

$$\omega_i = \frac{(2n-1)\,\pi c_0}{2L} \tag{151}$$

Similarly, for transversal vibrations, considering $v(x,t) = \phi(x)Z(t)$ the displacements in the transversal direction of a bar with E-modulus, E, and inertia, I, the differential equation of motion (eliminating the time dependent behaviour, $Z(t)$) and solution for $\phi(x)$ are,

$$\frac{\mathrm{d}^4\phi(x)}{\mathrm{d}x^4} - \phi(x)\omega^2\frac{m}{EI} = 0 \tag{152}$$

$$\phi(x) = A\sinh(\alpha x) + B\cosh(\alpha x) + C\sin(\alpha x) + D\cos(\alpha x) \tag{153}$$

where ω is the circular frequency of the system for time-dependent behaviour, $Z(t)$ and $\alpha = \sqrt[4]{\omega^2\frac{m}{EI}}$.

For a cantilever bar with L length, fixed at one end and free in another, one have $\phi(x=0) = 0$, $\frac{\mathrm{d}^2\phi}{\mathrm{d}x}(x=0) = 0$, $\dot{\phi}(x=L) = 0$ and $\frac{\mathrm{d}^4\phi}{\mathrm{d}x}(x=L) = 0$ as boundary conditions and the following natural frequencies, ω_i, are obtained from,

$$\omega_i = \alpha_i^2\sqrt{\frac{EI}{m}} \tag{154}$$

where, for the first natural frequency, $\alpha_1 = \frac{1.875}{L}$.

As stated in §3.4.3, global viscous damping relies on an estimate of the natural system frequency. This estimate can be obtained by the Rayleigh quotient or by an analytical estimate, using equivalence to continuous beams.

For the analytical calculation of the dynamic properties, an equivalence between discrete model and continuous solution is presented in Figure 4.15 and Table 4.3 shows the equivalent properties. Using this equivalence for each case study, both dynamic properties for real masses and scaled masses are presented in Tables 4.4 and 4.5.

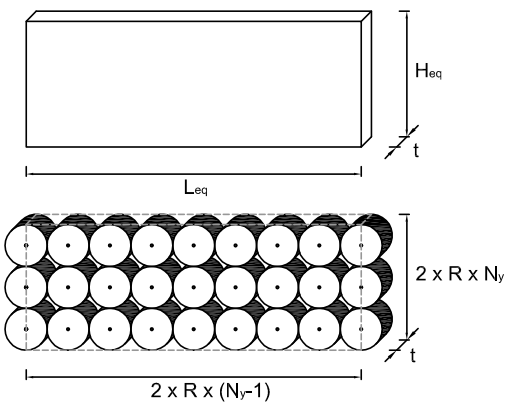

Figure 4.15 – Equivalence between discrete model and continuous beam

Table 4.3 – Equivalence between properties of analytical solution and properties of the test models

E_{eq}	A_{eq}	I_{eq}	L_{eq}	m_{eq}^{real}	m_{eq}^{scaled}
k_n	$2 \times R \times N_y \times t$	$\frac{t \times (2 \times R \times N_y)^3}{12}$	$2 \times R \times (N_x - 1)$	$\gamma \times A_{eq}$	$\frac{m_{scaled}^{1part.} \times N}{L_{eq}}$

In Figure 4.15 and in Table 4.3 N, N_x and N_y are the total number of particles, the number of particles in the horizontal axis and the number of particles in the vertical axis, respectively.

For the test models, Tables 4.4 and 4.5 show the values of the first natural frequency and the damping coefficient.

Table 4.4 – Dynamic properties of test models - real masses

Test model	ω_1 $[rad/s]$	c_c $[1/s]$	$c(\xi = 0.7/\xi = 0.2)$ $[1/s]$	Safety factor	ω_{ADR} $[rad/s]$	c_{ADR} $[1/s]$
2×1	0.46	0.92	0.64/0.18	1.0	0.43	0.87
2×2	5.9	11.8	8.3/2.4	1.2	1.11	2.22
20×5	0.1	0.2	0.1/0.04	1.2	0.005	0.010

Table 4.5 – Dynamic properties of test models - scaled masses

Test model	ω_1 $[rad/s]$	c_c $[1/s]$	$c(\xi = 0.7/\xi = 0.2)$ $[1/s]$	Safety factor	ω_{ADR} $[rad/s]$	c_{ADR} $[1/s]$
2×1	1.11	2.22	1.55/0.44	1.0	1.04	2.09
2×2	1.01	2.02	1.41/0.40	1.2	0.24	0.49
20×5	2.38	4.76	3.33/0.95	1.2	0.006	0.011

The following tables show the mechanical and dynamic properties and time step used for each analysis, considering real and scaled masses.

Table 4.6 – No damping model characteristics using critical time step

Model properties	m_{real}, I_{real}, k^{trans}, k^{rot}
Time step	Δt_{crit} - Eq. 51

Table 4.7 – No damping model characteristics using scaled masses

Model properties	m_{scaled}, I_{scaled}, k^{trans}, k^{rot}
Time step	$\Delta t = 1.0$

Table 4.8 – Global viscous damping model characteristics, using critical time step

Model properties	m_{real}, I_{real}, k^{trans}, k^{rot}
Time step	Δ_{crit} (Eq. 51)
Fundamental frequency	$\omega_0 = \omega_{analyt}$ (Eqs. 151, 154, Table 4.4)
Critical global damping coefficient	$c_c = 2\omega_{analyt} m_{real}$
Damping ratio	ξ (user-defined)
Global damping coefficient	$c = c_c \xi$ (Table 4.4)

Table 4.9 – Global viscous damping model characteristics, using density scaling

Model properties	m_{scaled}, I_{scaled} (Eqs. 57, 58), k^{trans}, k^{rot}
Time step	$\Delta_{crit} = 1.0$ sec
Fundamental frequency	$\omega_0 = \omega_{analyt} < 2.0$ (Eqs. 151, 154, Table 4.5)
Critical global damping coefficient	$c_c = 2\omega_{analyt} m_{scaled}$
Damping ratio	ξ (user-defined)
Global damping coefficient	$c = c_c \xi$ (Table 4.5)

Table 4.10 – Global viscous damping model characteristics, using adaptive dynamic relaxation and critical time step

Model properties	m_{real}, I_{real}, k^{trans}, k^{rot}
Time step	Δ_{crit} (Eq. 51)
Fundamental frequency	ω_0 (Rayleigh quotient: Eqs. 59, 60, 61)
Critical global damping coefficient	$c_c = 2\omega_{analyt} m_{real}$
Damping ratio	ξ (user-defined)
Global damping coefficient	$c = c_c \xi$ (Table 4.4)

Table 4.11 – Global viscous damping model characteristics, using adaptive dynamic relaxation and density scaling

Model properties	m_{scaled}, I_{scaled}, k^{trans}, k^{rot}
Time step	$\Delta_{crit} = 1.0$ sec
Fundamental frequency	$\omega_0 < 2.0$ (Rayleigh quotient: Eqs. 59, 60, 61)
Critical global damping coefficient	$c_c = 2\omega_{analyt} m_{scaled}$
Damping ratio	ξ (user-defined)
Global damping coefficient	$c = c_c \xi$ (Table 4.5)

4.2.2 Two particles in tension, one contact test

The first test to the code implementation is the case of two particles loaded in tension. Figure 4.16 shows the assembly, the boundary conditions and the loading conditions. The considered properties are defined in Tables 4.2, 4.4 and 4.5. The equilibrium state is represented in Figure 4.17 where the reactions and applied forces are shown, as well as the normal contact forces, using ParaView visualisation.

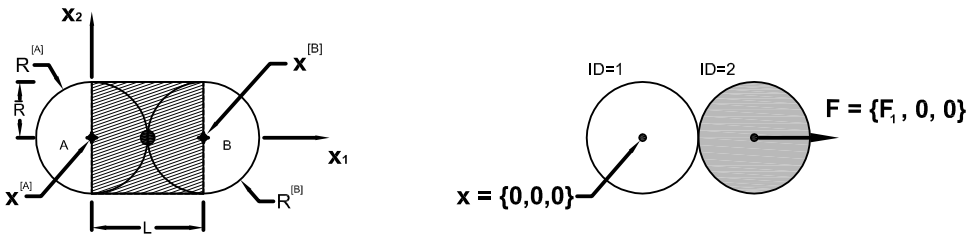

Figure 4.16 – Example 2×1 particles in pure tension

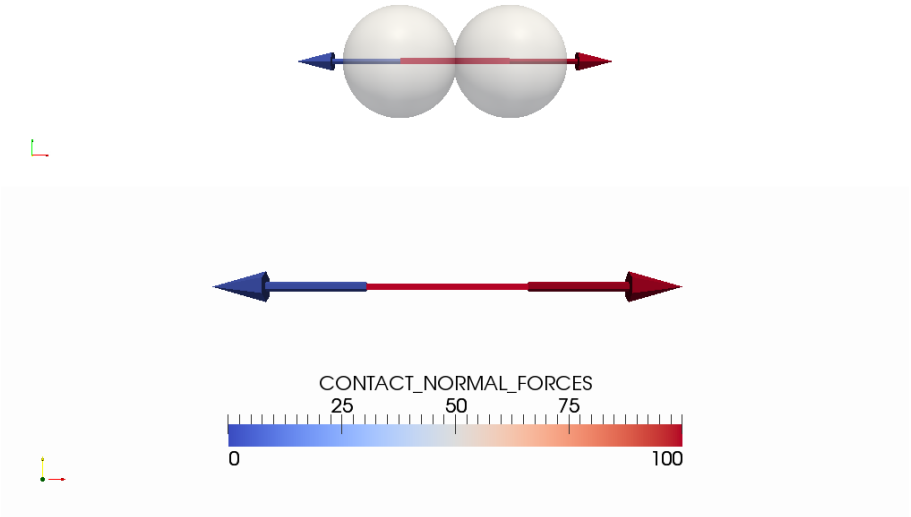

Figure 4.17 – Steady state for 2×1 particles in pure tension (red vector - reactions; blue vector - applied forces)

The results of the two particles in tension using real masses and the critical time step (Figure 4.18) and scaled masses and the unit time step (Figure 4.19) show the equivalence of the both analysis (results for the particle ID=2). The displacements oscillate between zero and 1.481×10^{-7} with and average value of 7.407×10^{-8}, which is the static solution for the structural system. The unbalanced forces oscillate also between $-100\ kN$ and $100\ kN$ since the system has no damping forces to reach equilibrium.

To obtain the steady state solution for the structural system and under given applied loadings, damping forces can be introduced. Figures 4.20, 4.21, 4.22 and 4.23 show the results of the two-particles mesh considering the global damping option for two user-defined damping ratio and for the adaptive dynamic relaxation (ADR). For a small damping ratio there are still some oscillatory behaviour around the static solution but, after 20 steps, the dynamic behaviour is reduced and a steady state regime is obtained,

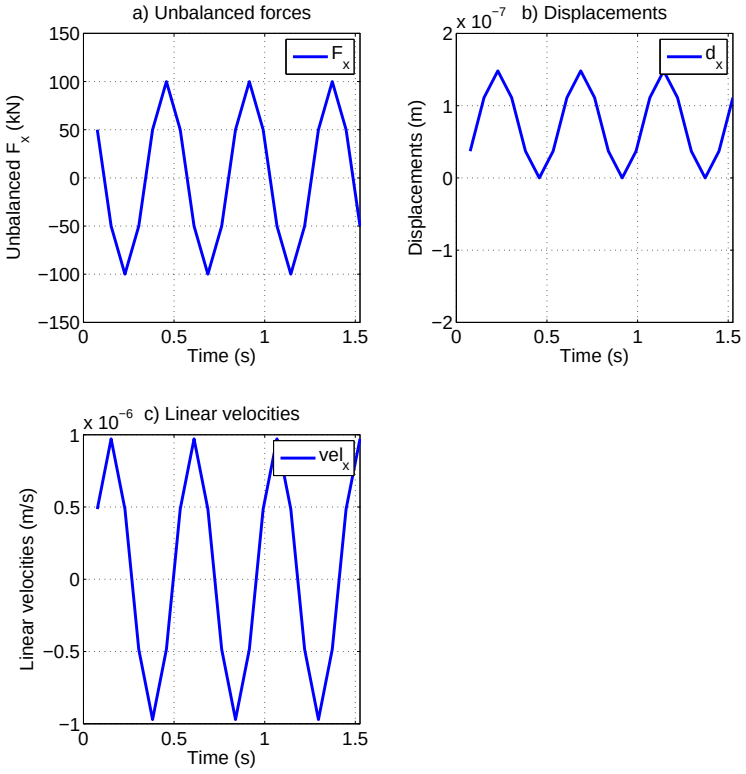

Figure 4.18 – Results for 2×1 particles in pure tension with no damping using real masses under applied force

where the unbalanced forces are close to zero. The adaptive dynamic relaxation for the two-particle example has a small overshooting of the solution due to the initial conditions (initial velocity obtained from an undamped system). Figure 4.24 shows the comparison between the different analyses using global damping. It is possible to verify the influence of the damping ratio on the development of displacements during stepping. The fastest convergence is obtained for the higher values of damping coefficient (≈ 1.0), i.e. for values of damping coefficients close to the critical damping coefficient.

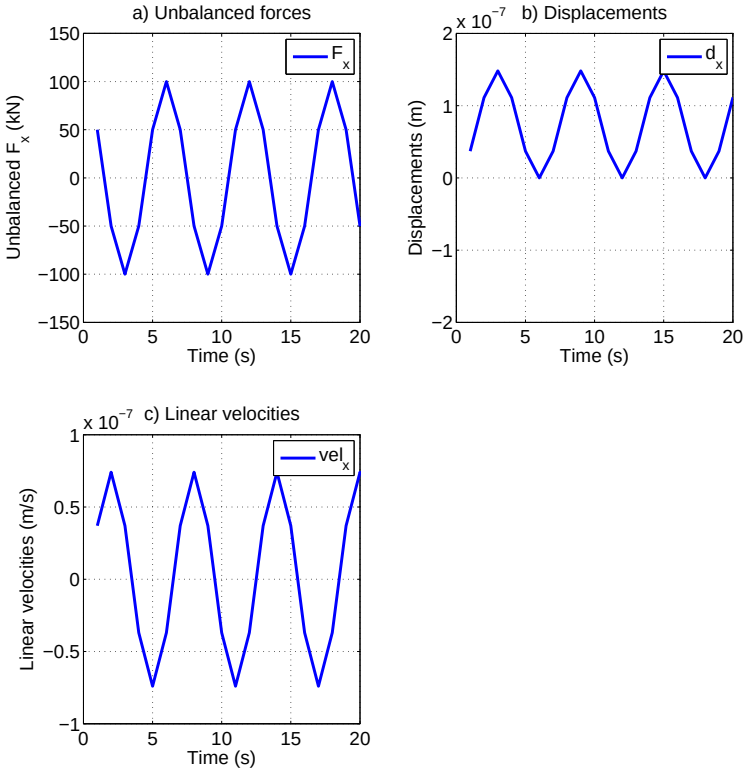

Figure 4.19 – Results for 2×1 particles in pure tension with no damping using scaled masses under applied force

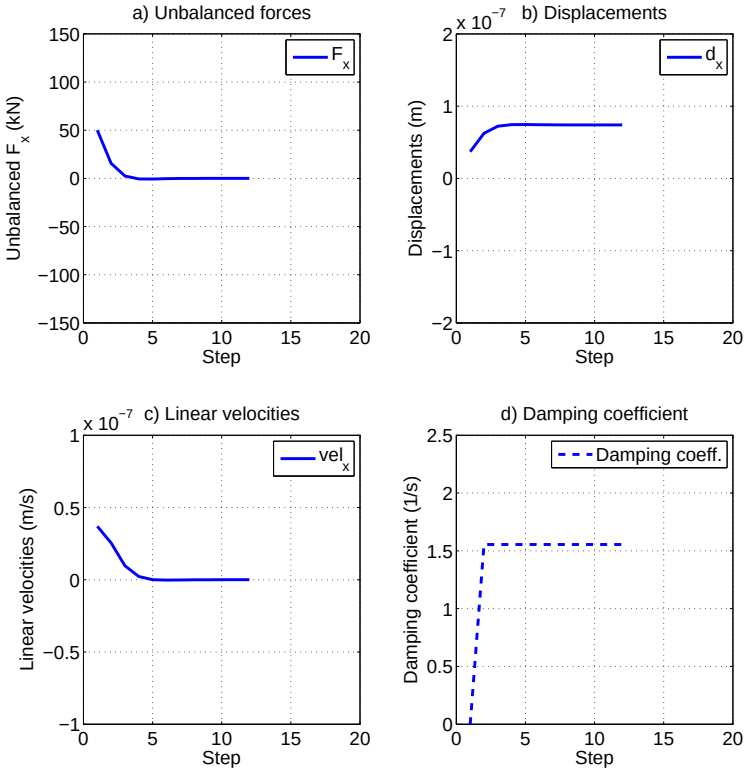

Figure 4.20 – Results for 2×1 particles in pure tension with global damping ($\xi = 0.7$) using scaled masses under applied force

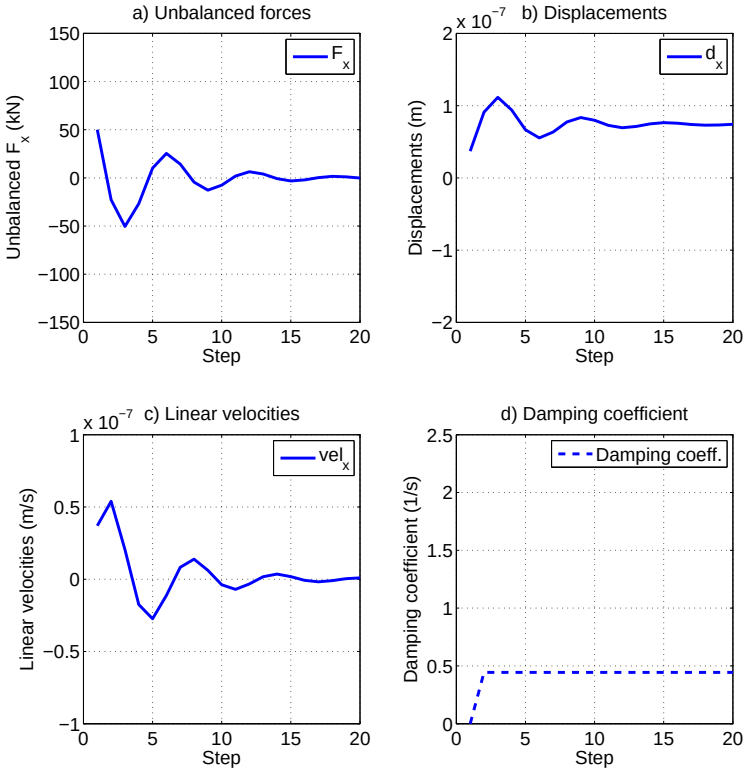

Figure 4.21 – Results for 2×1 particles in pure tension with global damping ($\xi = 0.2$) using scaled masses under applied force

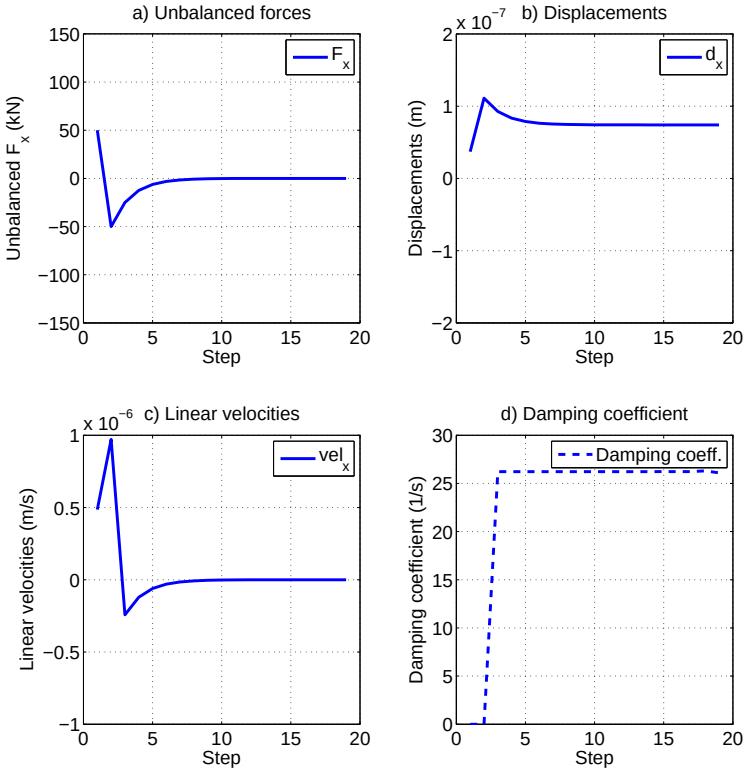

Figure 4.22 – Results for 2×1 particles in pure tension using adaptive dynamic relaxation (ADR) and real masses under applied force

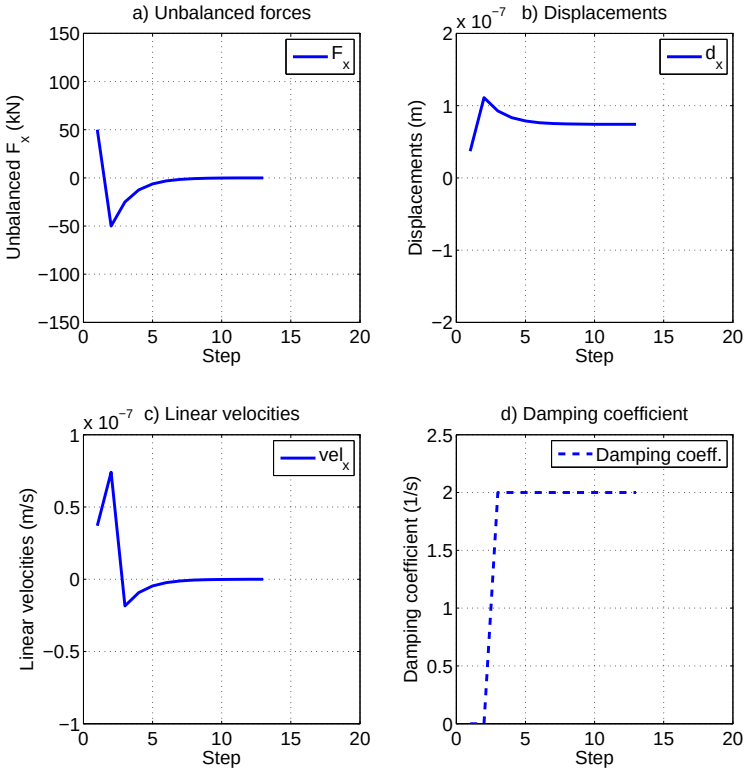

Figure 4.23 – Results for 2×1 particles in pure tension using adaptive dynamic relaxation (ADR) and scaled masses under applied force

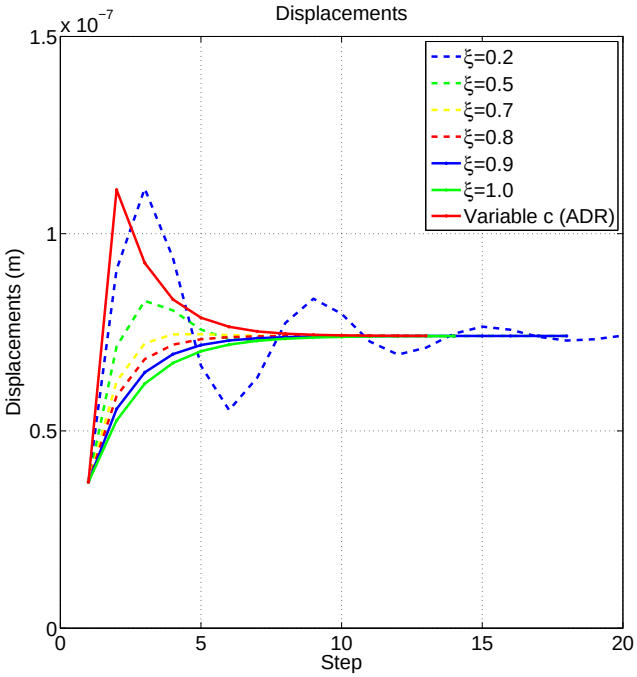

Figure 4.24 – Comparison of the results for 2×1 particles in pure tension using different global damping coefficients, adaptive dynamic relaxation under applied force and scaled masses

4.2.3 Four particles in shear test

The second test corresponds to the example of four particles loaded in shear. Figure 4.25 shows the assembly, the boundary conditions and the loading conditions. The considered properties are defined in Tables 4.2, 4.4 and 4.5. The equilibrium state is represented in Figure 4.26 where the reactions and applied forces are shown, as well as the normal contact forces. Similarly to the two-particle example, the main results for each analysis are presented in Figure 4.27 to Figure 4.30. Figure 4.31 shows the comparison between the different analyses using global damping and ADR, where the efficiency of the ADR method is demonstrated. The number of calculation steps necessary for convergence to the static solution of the similar to the number of steps obtained with the critical damping coefficient.

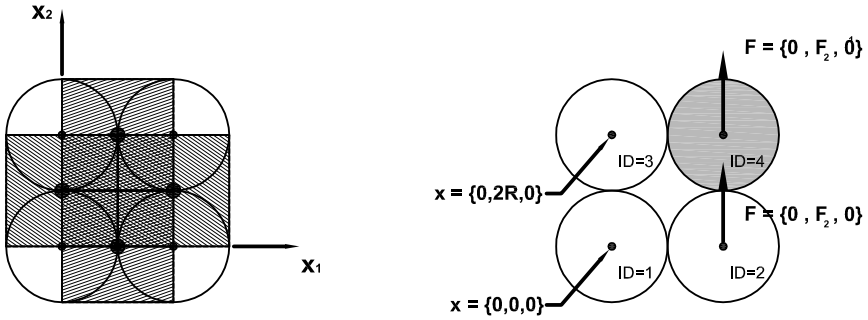

Figure 4.25 – Example 2×2 particles in pure shear, rectangular mesh

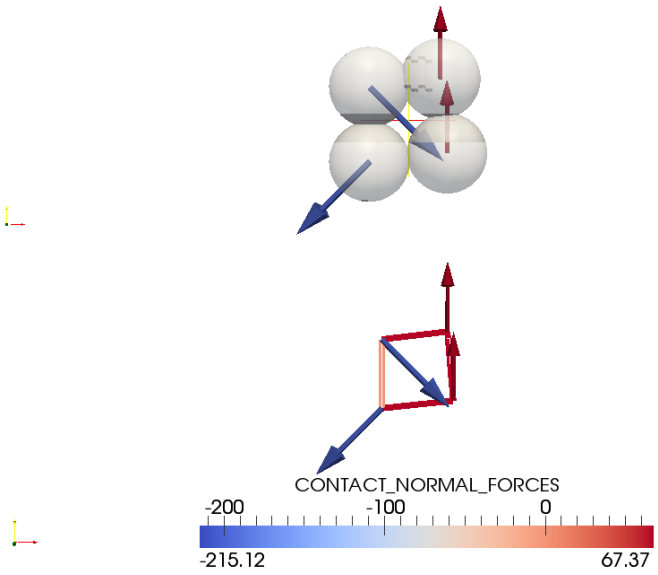

Figure 4.26 – Equilibrium state for 2×2 particles in pure shear (red vector - reactions; blue vector - applied forces)

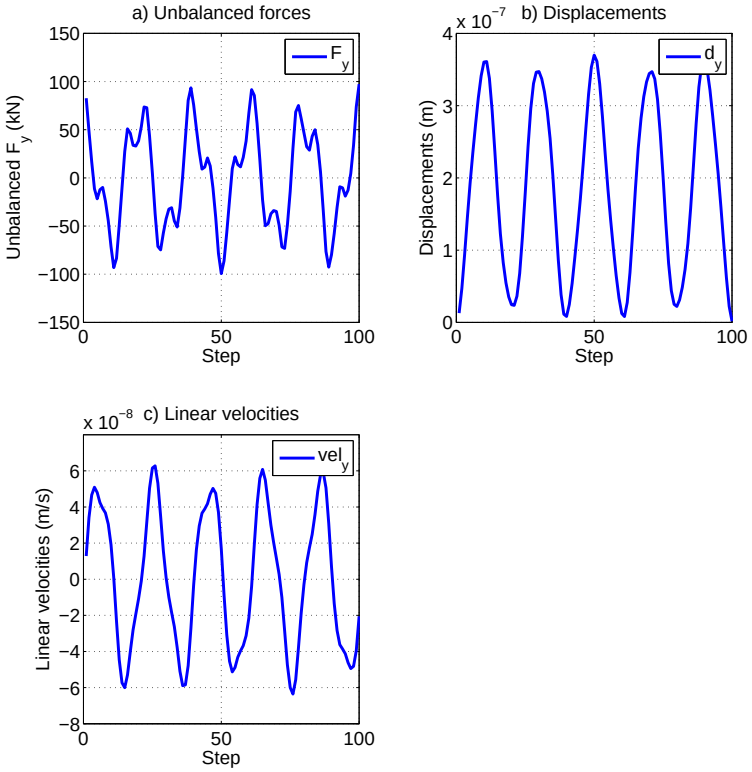

Figure 4.27 – Results for 2×2 particles in pure shear with no damping using scaled masses under applied forces

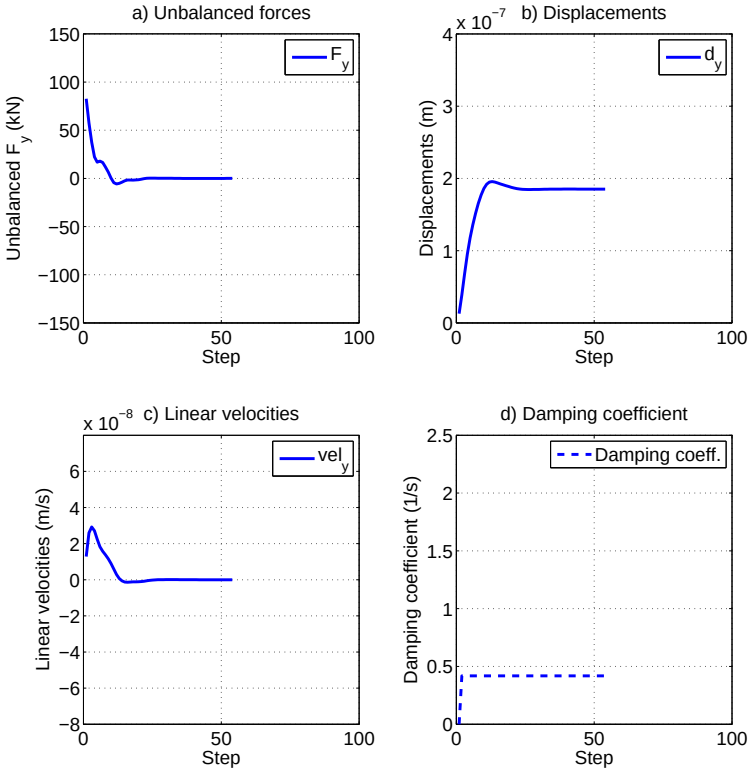

Figure 4.28 – Results for 2×2 particles in pure shear using global damping ($\xi = 0.7$) and scaled masses under applied forces

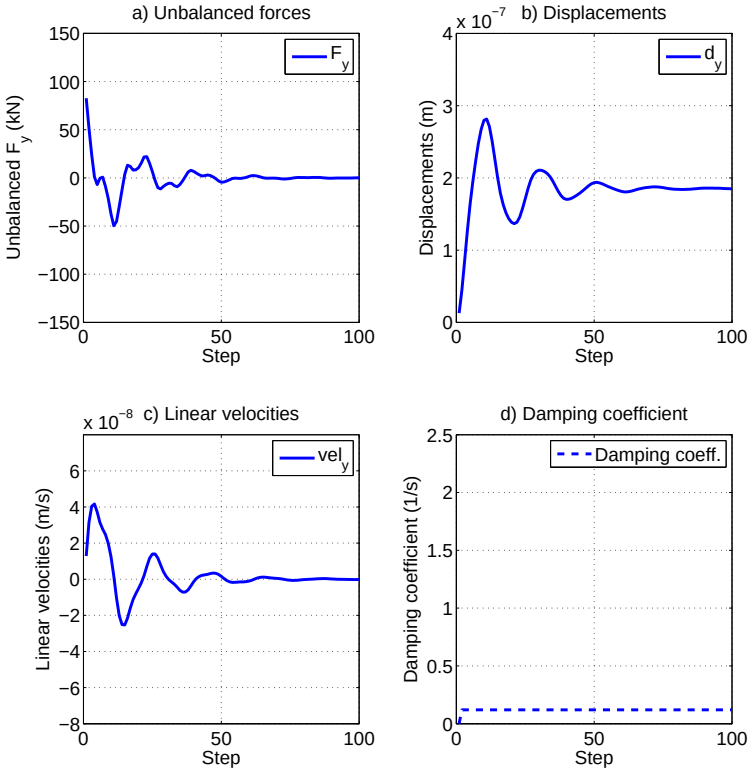

Figure 4.29 – Results for 2×2 particles in pure shear using global damping ($\xi = 0.2$) and scaled masses under applied forces

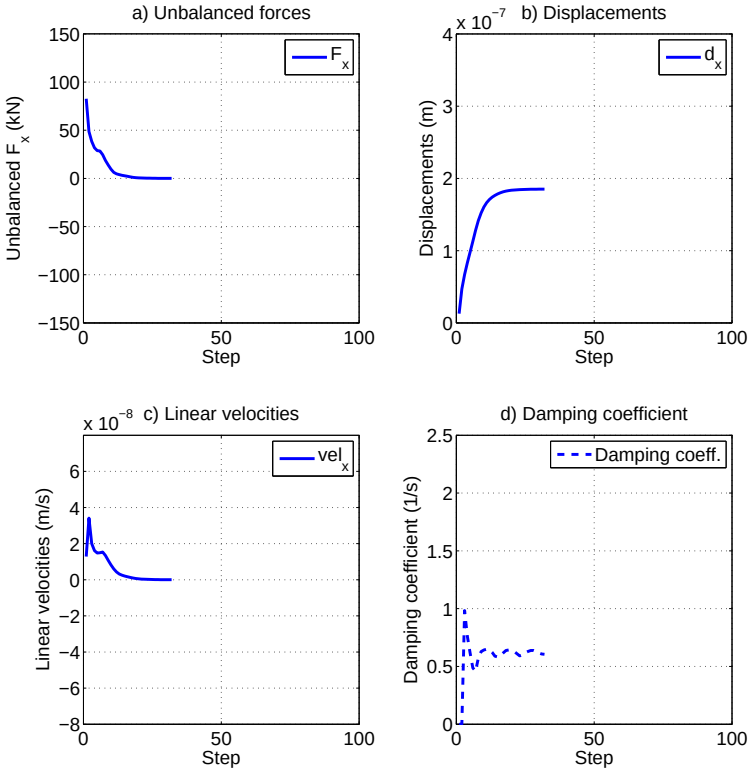

Figure 4.30 – Results for 2×2 particles in pure shear using adaptive dynamic relaxation (ADR) and scaled masses under applied forces

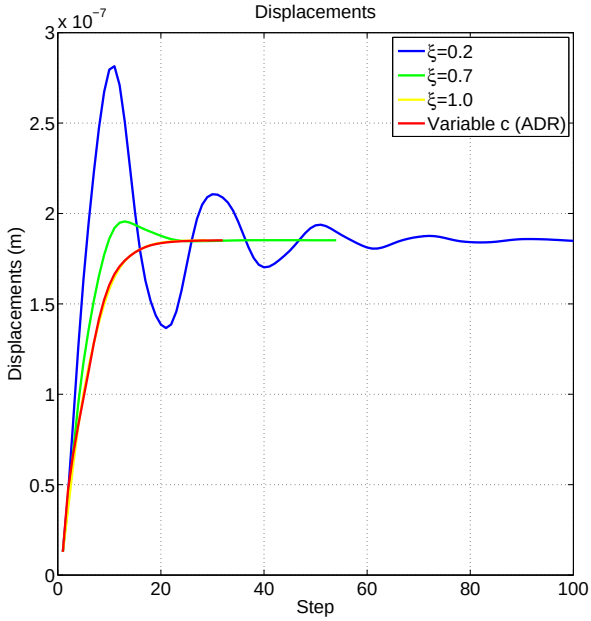

Figure 4.31 – Results for 2×2 particles in pure shear using different global damping coefficients, adaptive dynamic relaxation and scaled masses

4.2.4 Regular cantilever beam test

The third test uses one-hundred particles assembly in bending. Figures 4.32 shows the rectangular assembly, the boundary conditions and the loading conditions. The considered properties are defined in Tables 4.2, 4.4 and 4.5. The steady state is represented in Figures 4.26 and 4.33b where the reactions and applied forces are shown, as well as the normal contact forces, for the rectangular mesh and the hexagonal mesh. Similarly to the two-particle example, the main results for each analysis are presented in Figure 4.34 to Figure 4.36.

Figure 4.37 shows the main results of the analysis using the local damping, where the damping forces are calculated as a function of the particle force and applied to the system in the motion law with the reverse sign decreasing the velocities at each time-step.

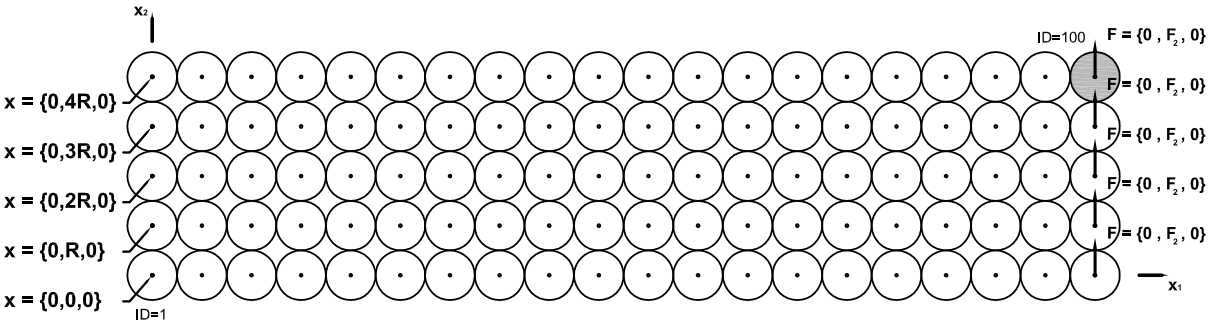

Figure 4.32 – Example 20×5 particles in bending, rectangular mesh

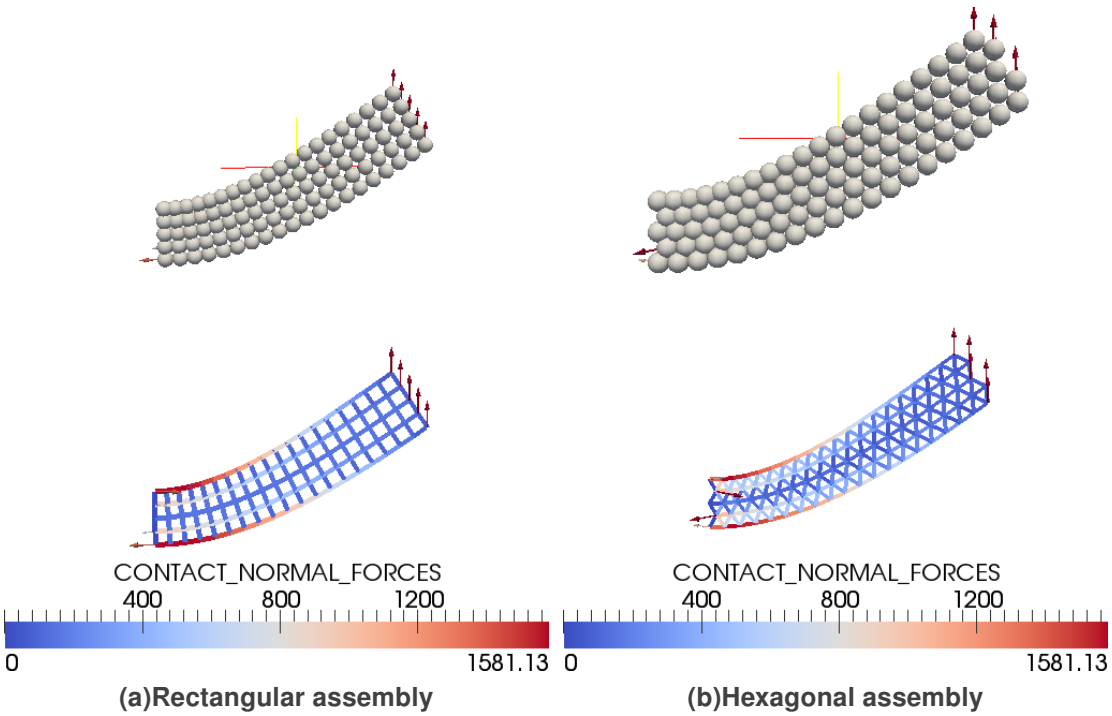

(a)Rectangular assembly **(b)Hexagonal assembly**

Figure 4.33 – Results for 20×5 particles in bending

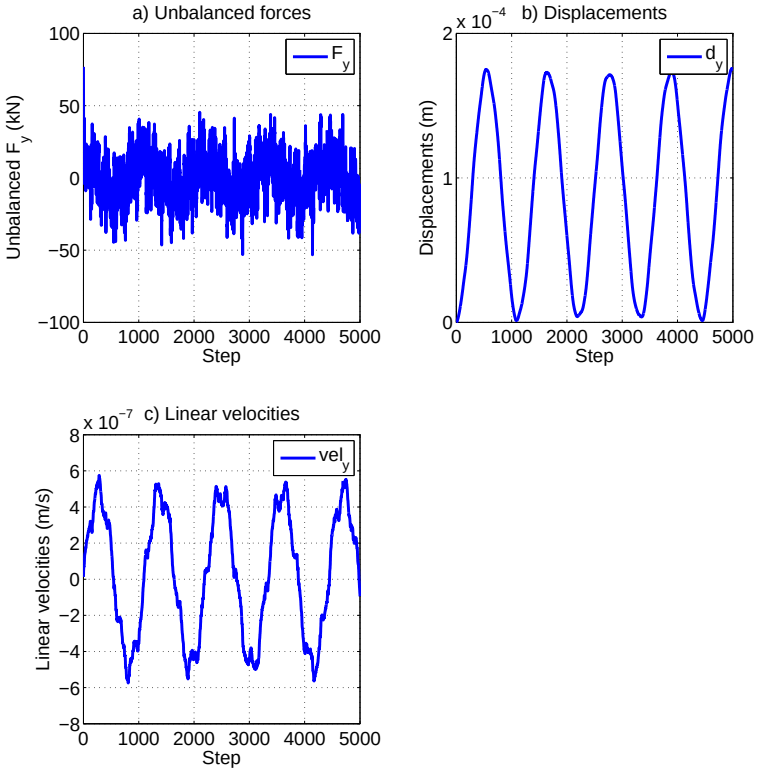

Figure 4.34 – Results for 20×5 particles in bending with no damping using scaled masses under applied forces

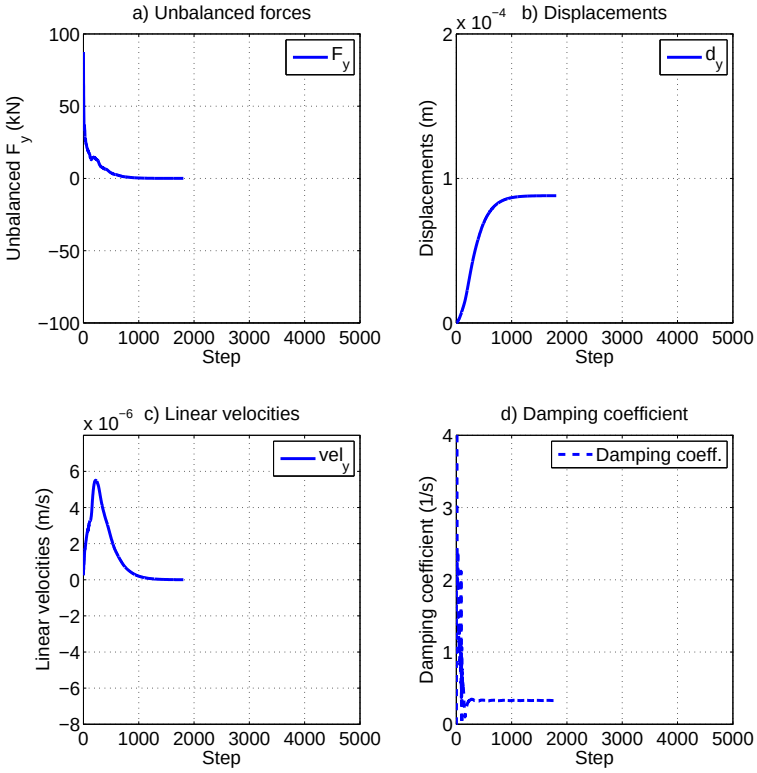

Figure 4.35 – Results for 20×5 particles in bending using adaptive dynamic relaxation (ADR) and real masses under applied forces

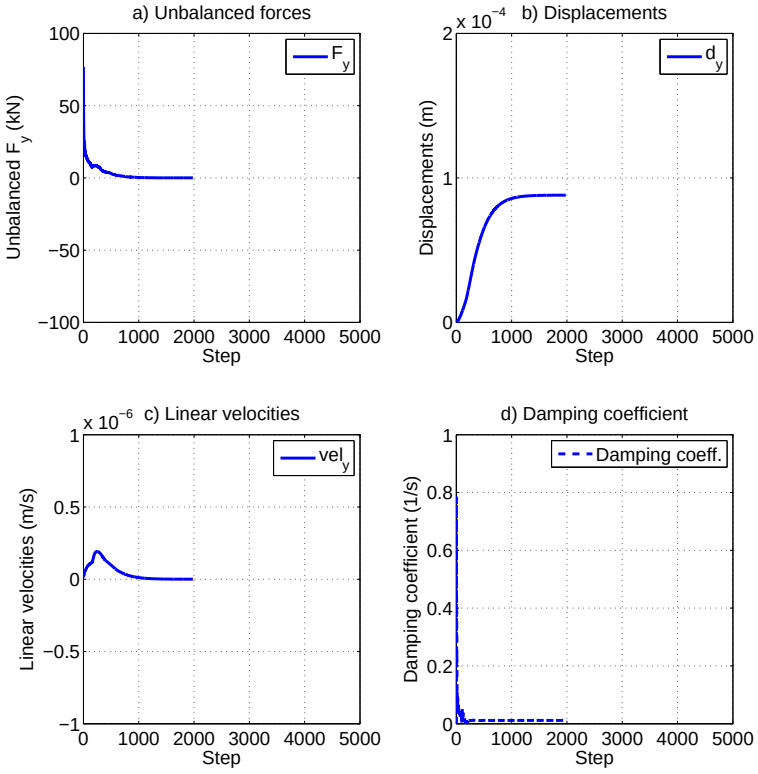

Figure 4.36 – Results for 20×5 particles in bending using adaptive dynamic relaxation (ADR) and scaled masses under applied forces

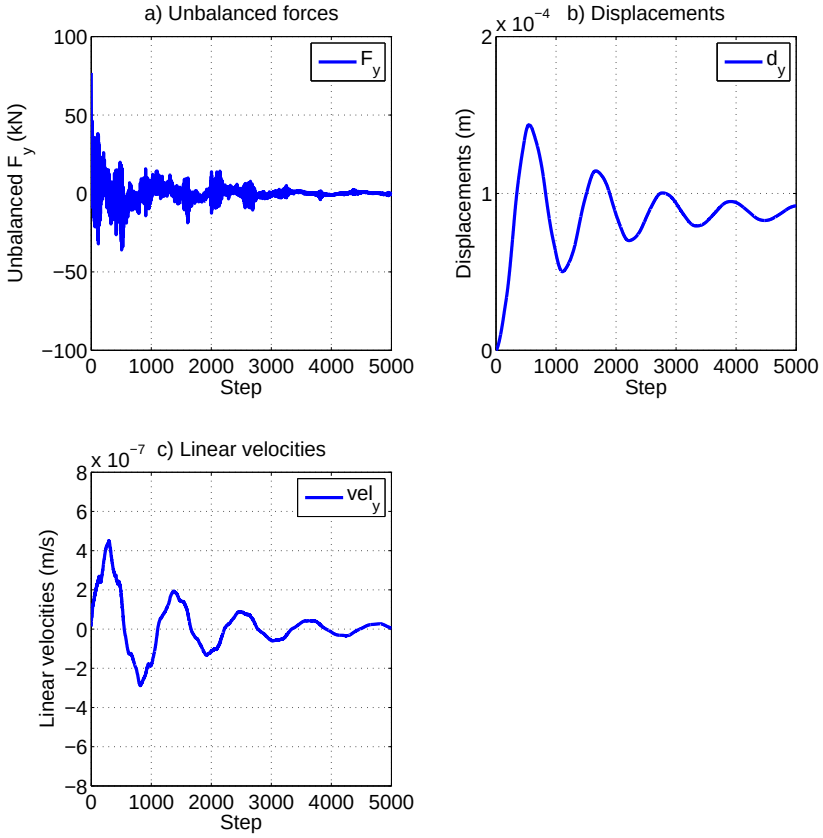

Figure 4.37 – Results for 20×5 particles in bending with local damping ($\alpha = 0.2$) and scaled masses under applied forces

4.3 Verification test for the cantilever beam with elastic behaviour

4.3.1 General aspects

Using the cantilever beam test, this section includes a theoretical example for the verification of the discrete method for the elastic analysis considering: i) beam equivalence; ii) elasticity theory; and iii) energy method.

4.3.2 Beam equivalence

The rectangular assembly used for this verification has 20×5 particles with a radius of $50\ m$ therefore, the equivalence between micro and macro properties follows,

$$k^n = \frac{EA}{L} = E \tag{155}$$

$$k^s = \frac{12EI}{L^3} = E \tag{156}$$

For simplicity k^n and k^s will be considered to be $10.0 \times 10^9\ kN/m$. This assembly with an applied vertical force of $200\ kN$ for each particle at the tip of the cantilever (5 particles) has a vertical displacement of $2.373 \times 10^{-5}\ kNm$.

The example used can be considered as a length of $(20-1) \times 50 \times 2 = 1900\ m$ and $5 \times 50 \times 2 = 500\ m$ height beam with a width of 1 and a load of $5 \times 200 = 1000\ kN$ at the tip of the beam. It is assumed a modulus of elasticity equivalent to the k^n and k^s considered for the former examples.

According to the theory of elasticity the deflection at the tip of the beam ($I_{beam} = \frac{1.0 \times 500^3}{12} = 1.04 \times 10^7\ m^4$) is given by,

$$\delta = \frac{FL_{beam}^3}{3EI_{beam}} = \frac{1000 \times 1900^3}{3 \times 10.0 \times 10^9 \times 1.04 \times 10^7} = 2.194 \times 10^{-5} m \tag{157}$$

The difference between discrete model and elastic theory is approximately 8.1%.

A refinement of the particle assembly results in a decrease of the difference between DEM displacement and analytical displacement. Table 4.12 shows the results for different particle assemblies and the difference to analytical beam displacement. The difference decreases significantly for assemblies with smaller particles.

4.3.3 Elasticity theory

Using the same model characteristics as before, the microparameters according to the elasticity theory, follow from the Equations (71), (72), (73) and (74).

Table 4.12 – Beam equivalence for different assembly refinements

Assembly	d_y - DEM (m)	d_y - Analytical (m)	Difference
20×5	2.37×10^{-5}		8.2%
39×5	2.30×10^{-5}	2.194×10^{-5}	4.9%
77×20	2.28×10^{-5}		3.8%

$$E' = \frac{E}{1-\nu^2} = 10.42 \times 10^9 \; kN/m \tag{158}$$

$$E'' = \frac{E}{2\,(1-\nu^2)} = 4.17 \times 10^9 \; kN/m \tag{159}$$

$$k^n = \frac{E'h}{L}t = E' \tag{160}$$

$$k^s = \frac{E''h}{L}t = E'' \tag{161}$$

The vertical displacements for the rectangular assemblies, with different refinements, using the calculated microparameters are given in Table 4.13.

Table 4.13 – Elasticity theory approximation for different assembly refinements

Assembly	d_y - DEM (m)	d_y - Analytical (m)	Difference
20×5	2.410×10^{-5}		9.8%
39×5	2.339×10^{-5}	2.194×10^{-5}	6.6%
77×20	2.318×10^{-5}		5.7%

4.3.4 Energy method

According to an equivalence of strain energy [Murat et al., 1992; Masuya et al., 1994], for hexagonal arrangement of particles, the contact stiffness can be defined as,

$$k_n = \frac{\sqrt{3}}{3\,(1-\nu)}E = 7.22 \times 10^9 \; kN/m \tag{162}$$

$$k_s = \frac{\sqrt{3}\,(1-3\nu)}{3\,(1-\nu^2)}E = 2.41 \times 10^9 \; kN/m \tag{163}$$

The vertical displacements for the hexangular assembly using the calculated microparameters are shown in Table 4.14. The analytical solution was obtained for an equivalent beam considering the height of the

hexangular assembly ($H = 446.41\ m$).

Table 4.14 – Energy method approximation for different assembly refinements

Assembly	d_y - DEM (m)	d_y - Analytical (m)	Difference
20×5	3.909×10^{-5}		26.8%
39×5	3.694×10^{-5}	3.084×10^{-5}	19.8%
77×20	3.566×10^{-5}		15.6%

4.4 Viscoelastic behaviour - Burger model

4.4.1 General aspects

For the viscoelastic behaviour using the Burger's model similar tests were made to verify the code implementation. The model properties are presented in Table 4.15.

Table 4.15 – Mechanical properties of Burger's model testing examples

radius $[m]$	**specific mass** $[ton/m^3]$	E_M $[kN/m]$	η_M $[kNs/m]$	E_K $[kN/m]$	η_K $[kNs/m]$	F $[kN]$	v $[m/s]$
0.05	2600	1.0×10^6	1.0×10^7	1.0×10^6	1.0×10^6	1000	0.001

4.4.2 Two particles in tension, one contact test

The first test to the code implementation is the case of two particles loaded in tension and under an imposed velocity. Figure 4.16 shows the assembly, the boundary conditions and the loading conditions. The considered properties are defined in Table 4.15. The main results are presented in Figure 4.38 and Figure 4.39. For this example a comparison with a DEM simulation using Particle Flow Code 2D, PFC2D [Itasca Consulting Group Inc., 2008], was made. The Burger's model is available in PFC2D as a constitutive model of the interaction between contacts and, therefore, it was possible to verify the code implementation, for both applied forces and imposed velocities in particle ID=2. The PFC2D uses a local damping for obtaining the steady state solution (default value of α=0.7). For this comparison, the real masses were used and a time step of $0.001\ sec$ was considered.

The results show that, considering no damping, the solution has an oscillatory behaviour during a long period of time and overshoots the analytical solution (§3.9.2). Using a combined adaptive dynamic relaxation method applied to the Burger's model, the system's response is close to the analytical solution (except for the first steps) and does not overshoot the solution. The PFC2D response, using local damping, has an oscillatory behaviour during the first period of time.

For this example of two-particles, using Burger's model, an imposed velocity was applied to the particle ID=2 and the obtained solution validates the code implementation, since it follows the analytical solution given in §3.9.2, for imposed displacements (Figure 4.40).

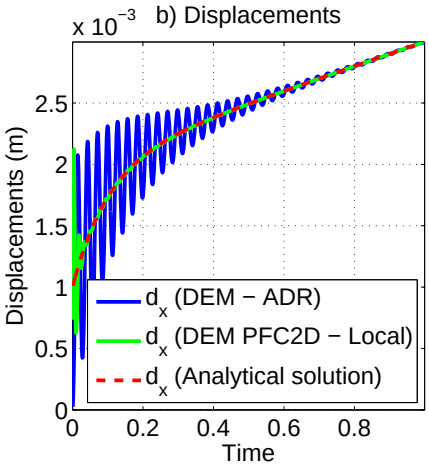

Figure 4.38 – Results for 2×1 particles in pure tension with no damping and real masses for applied forces

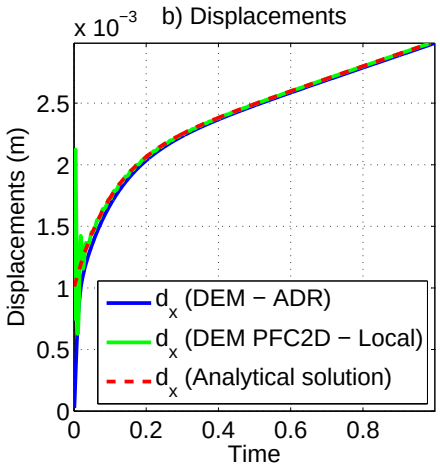

Figure 4.39 – Results for 2×1 particles in pure tension using adaptive dynamic relaxation (ADR) and real masses for applied forces

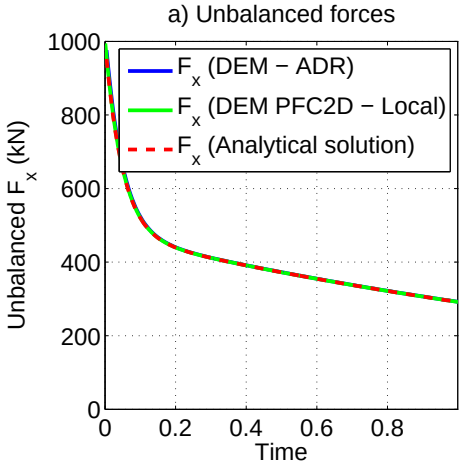

Figure 4.40 – Results for 2×1 particles in pure tension using adaptive dynamic relaxation (ADR) and real masses for imposed velocity

4.4.3 Four particles in shear test

The second example is the case of four particles loaded in shear. Figure 4.25 shows the assembly, the boundary conditions and the loading conditions. The considered properties are defined in Table 4.15. The main results are presented in Figure 4.41 and Figure 4.42.

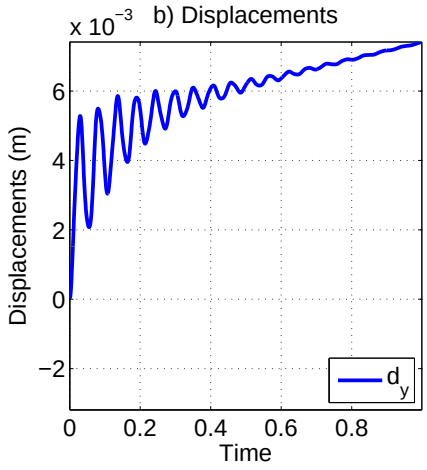

Figure 4.41 – Results for 2×2 particles in pure tension with no added damping using real masses under applied forces

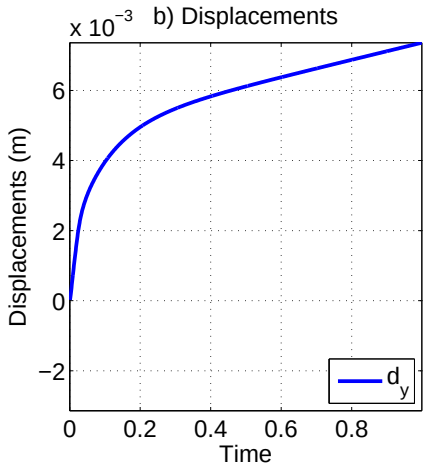

Figure 4.42 – Results for 2×2 particles in pure tension using adaptive dynamic relaxation (ADR) and real masses under applied forces

4.4.4 Regular cantilever beam test

The third example is the case of one-hundred particles loaded in bending. Figure 4.32 shows the assembly, the boundary conditions and the loading conditions. The considered properties are defined in Table 4.15. The main results are presented in Figure 4.43 and Figure 4.44.

The results show that the use of adaptive dynamic relaxation introduces a transition period where the system is being damped to the steady state solution (but it does not represents the actual viscoelastic behaviour, Figure 4.44).

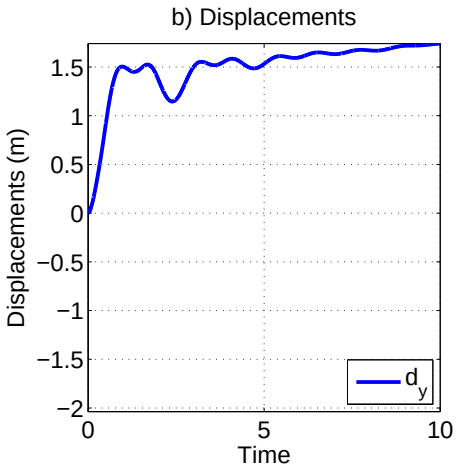

Figure 4.43 – Results for 20×5 particles in pure tension with no damping and real masses for applied forces

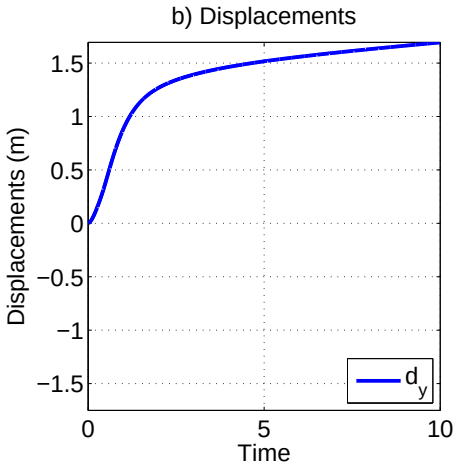

Figure 4.44 – Results for 20×5 particles in pure tension using adaptive dynamic relaxation (ADR) and real masses for applied forces

4.5 Aging model based on the solidification theory

4.5.1 General aspects

The aging model based on the solidification theory was implemented in order to take into account the delayed behaviour of concrete. Two basic examples show the response of the implementation, in pure tension and in bending. The properties of the aging model were obtained from the available data from the experimental work of Rostasy et. al. (available in [Bažant and Prasannan, 1989a]) and fitted to the model proposed by the solidification theory . The model parameters are presented in Table 4.16.

Table 4.16 – Mechanical properties of aging model based on solidification theory testing examples

radius $[m]$	**specific mass** $[ton/m^3]$	t' $[days]$	q_1 $[\times 10^{-6}/MPa]$	q_2 $[\times 10^{-6}/MPa]$	q_3 $[\times 10^{-6}/MPa]$	q_4 $[\times 10^{-6}/MPa]$	F $[kN]$	v $[m/s]$
0.05	2600	28	5.961	9.311	3.539	3.336	1000	0.001

As stated in § 3.9.5, the rate-type formulation of the aging model given by solidification theory implies the determination of the parameters of a nonaging Kelvin chain related with development of the viscoelastic microcompliance, $\Phi(t)$, following the described procedure. Figures 4.45 and 4.46 show the contribution of each Kelvin chain into the definition of the nonaging microcreep compliance of the solidifying material and the fit to the Rostasy et. al. creep data from 1971 [Bažant and Prasannan, 1989a].

Table 4.17 – Parameters of the Kelvin chain model for the creep compliance, $\Phi(t-t')$

Kelvin element, i	**Retardation time,** τ^i $[days]$	**Kelvin modulus,** $1/E^i(t_0)$ $[1/MPa]$
1	5.0×10^{-6}	4.7222×10^{-7}
2	0.5	1.0133×10^{-6}
3	5.0	1.1370×10^{-6}
4	50	1.2589×10^{-6}
5	500	1.3761×10^{-6}
6	5000	1.4858×10^{-6}

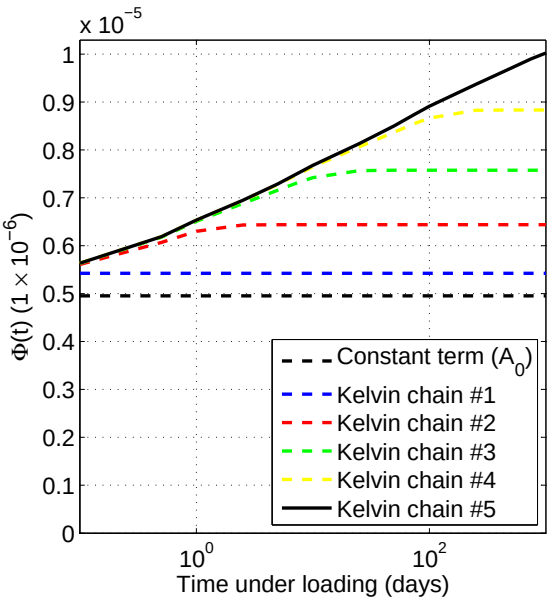

Figure 4.45 – Kelvin chain contributions to the nonaging viscoelastic compliance, $\Phi(t-t')$ related to Rostasy et. al. creep data

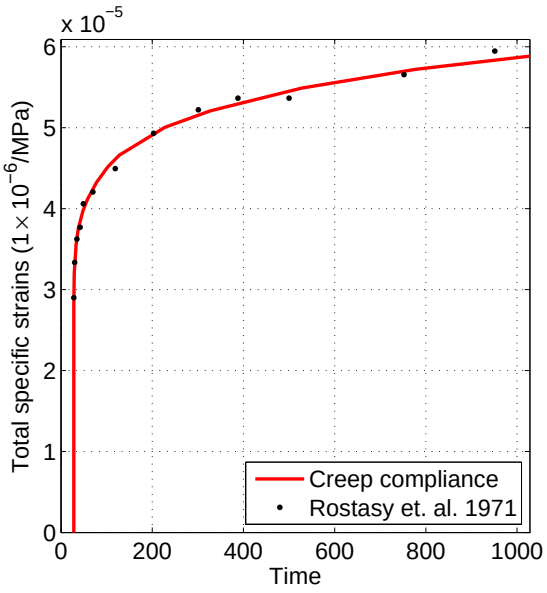

Figure 4.46 – Fit of the solidification theory rate-type form to the Rostasy et. al. creep data

4.5.2 Two particles in tension, one contact test

The first test to the code implementation is the case of two particles loaded in tension. Figure 4.16 shows the assembly, the boundary conditions and the loading conditions. The considered properties are defined in Tables 4.16 and 4.17. The main results are presented in Figure 4.47 and Figure 4.48.

Using the combined adaptive dynamic relaxation method applied to the aging model based on the solidification theory, the system's response is close to the analytical solution and does not overshoot the solution (Figure 4.47).

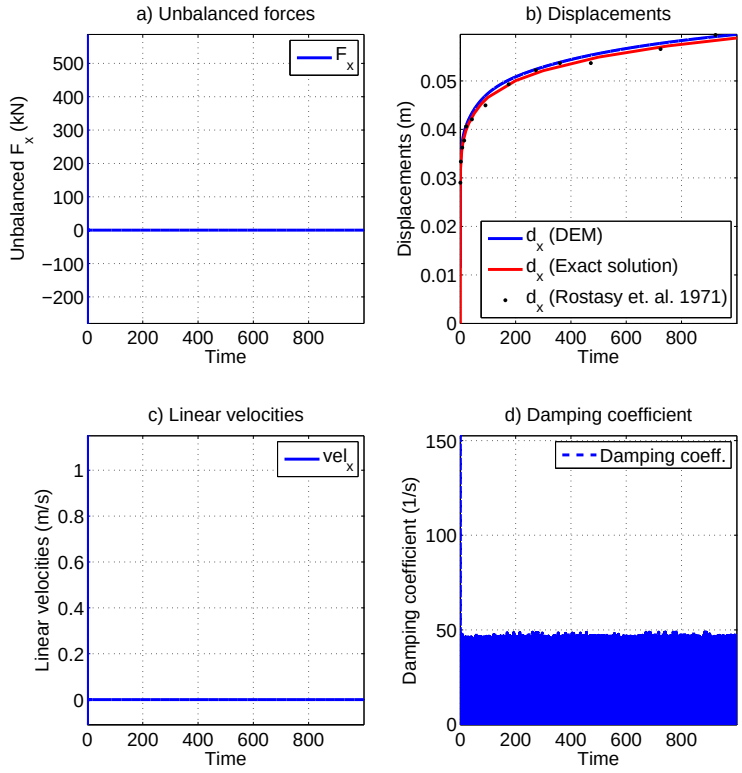

Figure 4.47 – Results for 2×1 particles in pure tension using ADR and real masses for applied force

4.5.3 Regular cantilever beam test

The second test was is the case of a bending cantilever, with one-hundred particles, 20× 5 (Figure 4.32). The model properties and forces were taken similar to the former test example and Figure 4.48 show the obtained results.

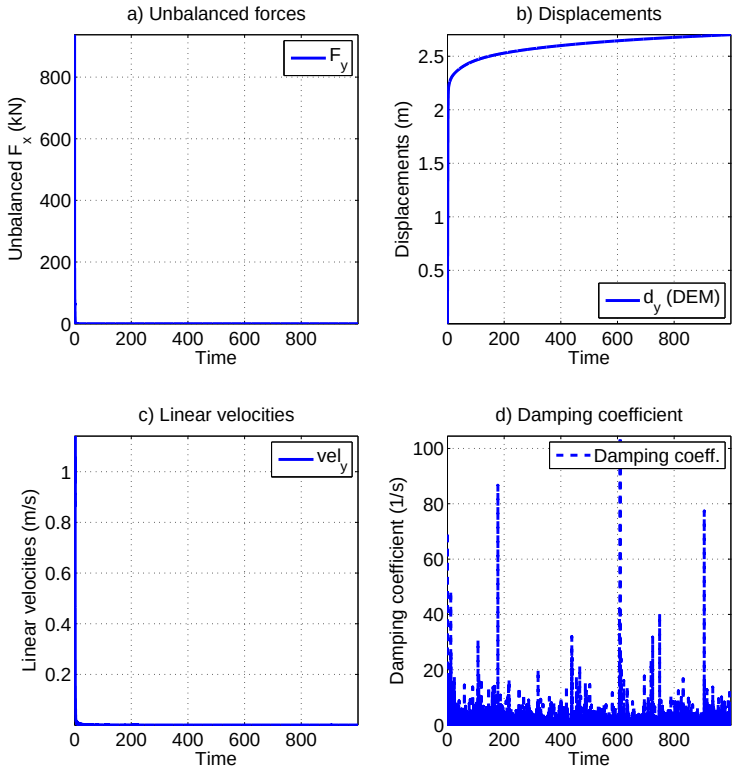

Figure 4.48 – Results for 2×1 particles in pure tension using ADR and real masses for applied force

4.6 Numerical incremental scheme for fast creep behaviour

4.6.1 General aspects

This section presents the results obtained for the numerical incremental scheme for fast creep behaviour simulation using DEM, described in §3.10 and based on the proposed procedure by Feng et al. [2003]. The advantage of this scheme is to obtain the response of a structural system with delayed behaviour over time, without the constraint of the critical time step used in the former examples. The maximum time step is usually very small and makes long term analysis to be very time consuming. The real time is discretized into predefined time steps, creep time steps, and for each step an adaptive dynamic relaxation procedure (described earlier) converges to the solution (using the critical time step or density scaling).

4.6.2 Burger model

The following example show the implementation for the numerical incremental scheme for fast creep behaviour based on the Burger's model applied to two particles in tension (Figure 4.49). The time was discretized into five creep time steps with the duration of 1 second (ΔT). The analysis was divided into two parts. The first introduced a large time step increment and an unbalanced force (Figure 4.49, after DT). Secondly, at each creep time step an adaptive dynamic relaxation (DR) is carried out in order to obtain a new equilibrium due to the introduced incremental forces (Figure 4.49, after DR). The results show that the equivalent DEM solution, using the incremental scheme, follows the analytical solution for each time step.

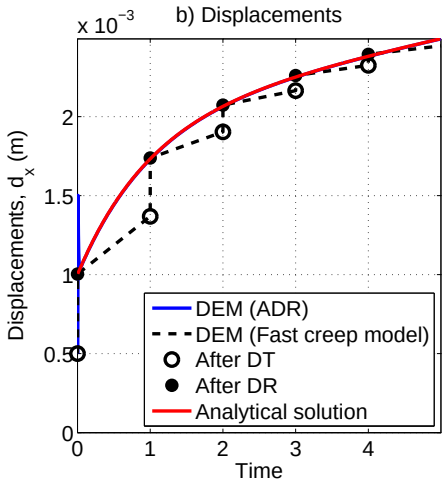

Figure 4.49 – Results for 2×1 particles in pure tension incremental scheme for fast creep solution

4.6.3 Solidification theory

The same type of result can be obtained for the aging model based on the solidification theory. Two examples are presented showing the normal and bending response of the structural systems (Figures 4.50 and 4.51).

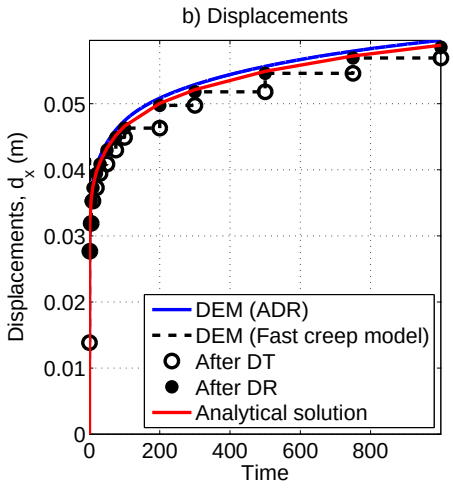

Figure 4.50 – Results for 2×1 particles in pure tension with no damping and real masses for applied force - comparison with equivalent solution

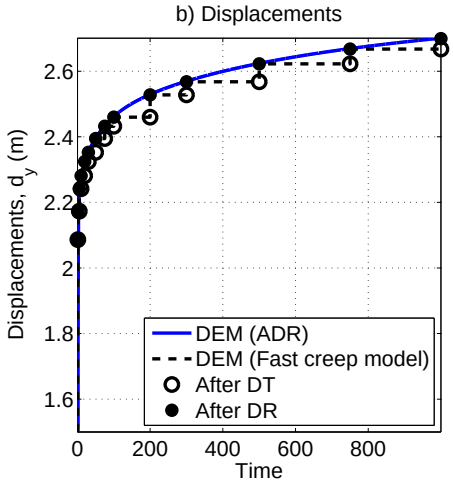

Figure 4.51 – Results for 20×5 particles in pure tension with no damping and real masses for applied force - comparison with equivalent solution

Table 4.18 shows the performance comparison between the two proposed methods for the time-dependent behaviour, the original DEM with ADR (small time steps) and the numerical incremental scheme for fast creep behaviour (large creep time steps). Considering the presented examples, the number of steps and the total calculation time decreases significantly using the fast creep model.

Table 4.18 – Comparison of performance results of the adaptive dynamic relaxation method (ADR) and of the numerical incremental scheme for fast creep model applied to the solidification theory

	2x1		25x5	
	ADR	Fast simulation	ADR	Fast simulation
Total loading time (days)	1000	1000	1000	1000
Time step ADR (days)	0.0216	0.0216	0.0084	0.0084
Total steps	46268	156	118969	13087
Total calculation time (min.)	15.9	≈ 0.0	42.5	2.3

5| Conclusions

The report presents a particle based discrete element method code implementation in C++ and constitutes a part of the Ph. D. thesis of the grant holder Carlos Serra, entitled "Experimental characterization and numerical modelling of dam concrete rheological properties", proposed in 2013 [Serra et al., 2013].

Firstly, a state of the art was presented, where several types of discrete models were briefly described, with special focus in the particle based models developed by Cundall. The third chapter details the concepts and numerical procedures implemented in the code, where the types of damping, the requirements for the solution stability and the density scaling approach were discussed. The testing examples were presented in the chapter four, in which standard testing examples were used to validate the code implementation for the different analysis options. The delayed behaviour was considered using a non-aging viscoelastic model, the Burger model, and an aging viscoelastic model based on the solidification theory. The code was also adapted in order to implement a numerical scheme for fast creep behaviour using both constitutive models applied to rigid particle models.

The literature review focused on the developments of discrete models, since its beginning in the early 70s by Cundall until more recent works, including the improvements to rigid particle models and the development of lattice models for the study of concrete behaviour.

The discrete element method considers two main procedures until convergence is obtained, the force-displacement law and the law of motion. The first governs the constitutive model applied to each particle contact and determines the interaction forces due to their relative displacements. The second law defines the kinematic of each element, defined by the motion differential equation. An explicit integration scheme was used to solve the differential equations and, therefore, procedures for the stability of the solution were studied and implemented. Different types of damping were described, an adaptive dynamic relaxation and a convergence criterion were also developed to insure a steady-state convergence, equivalent to the static solution.

Three types of time-dependent constitutive models were implemented in the scope of this work: the Hooke's model, the Burger's model and the aging model derived from the solidification theory. The ultimate objective was to introduce the delayed behaviour of aging materials, such as concrete, although the previous simpler models were used for the validation of the DEM code.

Since the explicit integration schemes require a small time step in order to obtain convergence, a numerical incremental scheme for fast creep behaviour simulation was developed in order to obtain the delayed behaviour over large periods of time, as it is usually required in concrete structures analysis. This numerical algorithm was developed for both Burger's model and for the aging model based on the solidification theory and showed a significant increase of computational efficiency when compared with the original DEM solution.

The validation of the DEM code was based on simple regular models representing tensile (2×1 particles),

shear (2×2 particles) and bending (20×5 particles) behaviour. Several types of analysis were performed, considering both real and scaled masses, global and local damping and the adaptive dynamic relaxation (ADR) and the three types of constitute models. The proposed numerical incremental scheme for fast creep was also validated for the main examples, considering large creep time steps (ΔT).

This work was developed for the doctoral course entitled *Elementos finitos em engenharia de estruturas* under Prof. Corneliu Cismasiu's supervision.

Lisboa, LNEC, julho de 2015

VISTOS

O Chefe do Núcleo de Observação

António Tavares de Castro

O Chefe do Núcleo de Modelação e Mecânica das Rochas

Luís Manuel Nolasco Lamas

O Diretor do Departamento de Barragens de Betão

António Lopes Batista

AUTORIA

Carlos Luís de Oliveira Serra
Bolseiro de Doutoramento

Nuno Monteiro Azevedo
Investigador Auxiliar

António Lopes Batista
Investigador Principal

References

Ayachit, U. (2005). “The ParaView Guide: A Parallel Visualization Application.

Azevedo, N. (2003). “A rigid particle discrete element model for the fracture analysis of plain and reinforced concrete.” Ph.d., Heriot-Watt University, Heriot-Watt University.

Azevedo, N. M., Lemos, J., and de Almeida, J. R. (2008). “Influence of aggregate deformation and contact behaviour on discrete particle modelling of fracture of concrete.” *Eng. Fract. Mech.*, 75(6), 1569–1586.

Bažant, Z. P. (1977). “Viscoelasticity of solidifying porous material - Concrete.” *J. Eng. Mech. Div.*, 103(6), 1049–1067.

Bažant, Z. P. (1988). “Material models for structural creep analysis.” *Math. Model. Creep Shrinkage Concr.*, Z. P. Bažant, ed., Wiley & Sons, Evanston, Chapter 2, 99–215.

Bažant, Z. P. (2002). *Scaling of structural strength*. Hermes-Penton Science, London, first edit edition.

Bažant, Z. P. and Baweja, S. (1995). “Creep and shrinkage prediction model for analysis and design of concrete structures - model B3.” *Mater. Struct.*, 28, 357–365.

Bažant, Z. P. and Baweja, S. (2000). “Creep and shrinkage prediction model for analysis and design of concrete structures - model B3.” *Adam Nev. Symp. Creep Shrinkage - Struct. Des. Eff.*, A. Al-Manaseer, ed., Vol. 28, Michigan, 1–83 (July).

Bažant, Z. P. and Chern, J. C. (1985a). “Log-double power law for concrete creep.” *ACI J.*, 82(59), 665–675.

Bažant, Z. P. and Chern, J. C. (1985b). “Triple power law for concrete creep.” *J. Eng. Mech.*, 111(1), 63–83.

Bažant, Z. P., Cusatis, G., and Cedolin, L. (2004). “Temperature Effect on Concrete Creep Modeled by Microprestress-Solidification Theory.” *J. Eng. Mech.*, 130(6), 691.

Bažant, Z. P. and Osman, E. (1976). “Double power law for basic creep of concrete.” *Mater. Struct. (RILEM, Paris)*, 9(49), 3–11.

Bažant, Z. P. and Prasannan, S. (1989b). “Solidification theory for concrete creep. I: Formulation.” *J. Eng. Mech.*, 115(8), 1691–1703.

Bažant, Z. P. and Prasannan, S. (1989a). “Solidification theory for concrete creep. II: Verification and application.” *J. Eng. Mech.*, 115(8), 1704–1725.

Bažant, Z. P., Tabbara, M. R., Kazemi, M. T., and Pijaudier-Cabot, G. (1990). “Random Particle Model for Fracture of Aggregate or Fiber Composites.” *J. Eng. Mech.*, 116(8), 1686–1705.

Bažant, Z. P. and Wu, S. T. (1973). “Dirichlet series creep function for aging concrete.” *J. Eng. Mech. Div.*, 99(2), 367–387.

Bažant, Z. P. and Xi, Y. (1995). "Continuous retardation spectrum for solidification theory of concrete creep." *J. Eng. Mech.*, 121(2), 281–288.

Belytschko, T. and Hughes, T. J. R. (1983). "Computational methods for transient analysis." *Mech. Math. Methods*, T. Belytschko and T. J. R. Hughes, eds., North Holland, 536.

Bolander, J. and Saito, S. (1998). "Fracture analyses using spring networks with random geometry." *Eng. Fract. Mech.*, 61(5-6), 569–591.

Clough, R. W. and Penzien, J. (1993). *Dynamics of structures*. McGraw-Hill Internation Editions, 2 edition.

Cundall, P. A. (1971). "A computer model for simulating progressive large scale movements in blocky rock systems." *Proc. Int. Symp. rock Fract.*, International Society for Rock Mechanics, ed., Nancy, 129–136.

Cundall, P. A. (1987). "Distinct element models of rock and soil structure." *Anal. Comput. methods Eng. rock Mech.*, E. T. Brown, ed., Allen & Unwin, London, Chapter 4, 129–163.

Cundall, P. A. and Strack, O. D. L. (1979). "A discrete numerical model for granular assemblies." *Géotechnique*, 29(1), 47–65.

Cusatis, G. (2001). "Tridimensional random particle model for concrete." Ph.d., Politecnico di Milano, Politecnico di Milano.

Feng, J., Chuhan, Z., Gang, W., and Guanglun, W. (2003). "Creep Modeling in Excavation Analysis of a High Rock Slope." *J. Geotech. Geoenvironmental Eng.*, 129(9), 849–857.

Findley, W., Lai, J., and Onaram, K. (1976). *Creep and relaxation of nonlinear viscoelastic materials: with an introdution to linear viscoelasticity*. Dover Publications, Inc., New York.

Hassani, N. (1998). "An experimental-numerical study for the determination of concrete fracture physical parameters in DEM." *Fract. Mech. Concr. Struct.*, Freiburg, Germany, AEDIFICATIO.

Itasca Consulting Group Inc. (2008). "PFC2D (Particle Flow Code in 2 Dimensions).

Kawai, T. (1978). "New discrete models and their application to seismic response analysis of structures." *Nucl. Eng. Des.*, 48(1), 207–229.

Lilliu, G. and van Mier, J. (2003). "3D lattice type fracture model for concrete." *Eng. Fract. Mech.*, 70(7-8), 927–941.

Mas Ivars, D., Pierce, M. E., Darcel, C., Reyes-Montes, J., Potyondy, D. O., Paul Young, R., and Cundall, P. A. (2011). "The synthetic rock mass approach for jointed rock mass modelling." *Int. J. Rock Mech. Min. Sci.*, 48(2), 219–244.

Masuya, H., Kajikawa, Y., and Nakata, Y. (1994). "Application of the distinct element method to the analysis of the concrete members under impact." *Nucl. Eng. Des.*, 150(2-3), 367–377.

Meguro, K. and Hakuno, M. (1989). "Fracture analysis of concrete structures by the modified distinct element method." *Struct. Eng. / Earthq. Eng.*, 6(2), 283–294.

Microsoft Corporation (2010). "Microsoft Visual C++ 2010 Express.

Murat, M., Anholt, M., and Wagner, H. D. (1992). "Fracture behavior of short-fiber reinforced materials." *J. Mater. Res.*, 7(11), 3120–3131.

Petrinic, N. (1996). "Aspects of Discrete Element Modelling Involving Facet-to-facet Contact Detection and Interaction." Ph.d., University of Wales Swansea, University of Wales Swansea.

Plesha, M. E. (1983). "On the modeling of rocks with microstructure." *24th U.S. Symp. Rock Mech.*, Station, Texas, American Rock Mechanics Association.

Potyondy, D. and Cundall, P. (2004). "A bonded-particle model for rock." *Int. J. Rock Mech. Min. Sci.*, 41(8), 1329–1364.

Rodríguez-Ortiz, J. M. (1974). "Estudio del comportamiento de medios granulares heterogéneos mediante modelos discontinuos analógicos y matemáticos." Ph.d. thesis, Universidad Politécnica de Madrid, Universidad Politécnica de Madrid.

Sauvé, R. G. and Metzger, D. R. (1995). "Advances in Dynamic Relaxation Techniques for Nonlinear Finite Element Analysis." *J. Press. Vessel Technol.*, 117(2), 170.

Schlangen, E. and van Mier, J. (1992). "Experimental and numerical analysis of micromechanisms of fracture of cement-based composites." *Cem. Concr. Compos.*, 14(2), 105–118.

Serra, C., Batista, A. L., and Azevedo, N. M. (2013). *Caracterização experimental e modelação numérica das propriedades reológicas do betão de barragens. Plano de tese de doutoramento do Bolseiro de Iniciação à Investigação Científica Carlos Serra*. Laboratório Nacional de Engenharia Civil, Lisboa.

Tavarez, F. A. and Plesha, M. E. (2007). "Discrete element method for modelling solid and particulate materials." *Int. J. Numer. Methods Eng.*, 70(4), 379–404.

Underwood, P. (1983). "Dynamic Relaxation." *Comput. Methods Transient Anal.*, Elsevier Science Publishers B.V., Chapter 5, 245–265.

Vieria de Lemos, J. (1987). "A distinct element model for dynamic analysis of jointed rock with application to dam foundations and fault motion." Ph.d., University of Minnesota, University of Minnesota.

Zubelewicz, A. and Mróz, Z. (1983). "Numerical simulation of rock burst processes treated as problems of dynamic instability." *Rock Mech. Rock Eng.*, 16(4), 253–274.